Fabrication of High-Temperature Superconducting nanobridges Using Atomic Force Microscopy

by

Akram Abdulsalam Elkaseh

Assignment presented at the University of Stellenbosch in partial fulfilment of the requirements for the degree of

Master of Engineering of Electrical and Electronic Engineering

Department of Electrical and Electronic Engineering

University of Stellenbosch

Private Bag X1, 7602 Matieland, South Africa

Supervisors:

Prof. W. J. Perold Dr. M. Meincken

October 2006

Declaration

I, the undersigned, hereby declare that the work contained in this assignment is my own original work and that I have not previously in its entirety or in part submitted it at any university for a degree.

Signature: ……..

A. A. Elkaseh

Date: ……..

Abstract

The Josephson effect of high-temperature superconducting nanobridge structures is studied worldwide. Until now, nanobridges are generally fabricated with focused ion beam milling on planar thin films. These nanobridges are employed as weak links in superconducting quantum interference devices (SQUIDs) and used in superconducting flux flow transistors and devices.

This project had two main objectives: to improve the sidewall angle of photoresist lines, with the aid of atomic force microscopy (AFM) nanolithography; and to fabricate high-temperature Josephson junctions by constricting superconductive YBCO lines on MgO substrates with AFM nanolithography. The entire fabrication process is explained including photolithography, deposition of the YBCO thin films with pulsed laser deposition (PLD), nanolithography and wet etching.

Although the testing of the junctions did not show any Josephson behaviour, it could be demonstrated that nanobridge structures can successfully be created by AFM nanolithography.
The entire fabrication process has been demonstrated in detail for the benefit of future research.

Opsomming

Die Josephson effek in hoë-temperatuur supergeleidende nanobrugstrukture word wêreldwyd bestudeer. Tot op hede is nanobrûe oor die algemeen deur middel van gefokusde ioonstraaletsing van dun films vervaardig. Hierdie nanobrûe word as swak skakels aangewend in supergeleidende kwantum interferensie toestelle (SQUIDs) asook in supergeleidende vloedvloei transistors en toestelle.

Hierdie projek het twee doelstellings voor oë gehad: om die sywandshoeke van fotoweerstandslyne te verbeter met behulp van atomiese krag mikroskopie (AFM), asook die vervaardiging van hoë-temperatuur Josephson skakels deur die vernouing van supergeleidende YBCO lyne op MgO substrate deur middel van AFM nanolitografie. Die hele vervaardigingsproses word verduidelik, onder meer fotolitografie, deposisie van die YBCO dunfilms met behulp van gepulseerde laser deposisie (PLD), nanolitografie en nat-etsing.

Alhoewel die toetse op die skakels geen Josephson gedrag getoon het nie, kon dit wel gewys word dat nanobrugstrukture suksesvol deur middel van AFM nanolitografie vervaardig kan word.
Die vervaardigingsproses word gedetailleer vir die doeleindes van toekomstige navorsing.

Acknowledgements

I would like to express my deep and sincere gratitude to a few people for helping me with my thesis.

I would like to thank Professor W. J. Perold for his patience and the positive advice that he always gave me. Thanks for your encouragement and help in the course of this thesis.

I would also like to thank Dr M. Meincken for her unlimited support and for sharing her superior knowledge of AFM.

My thanks will always go to my family who helped to keep me motivated. And special thanks to my wife Entisar for her patience and support during the period of my master's studies.

I would like also to thank the International Centre for macro Molecular Chemistry and Technology in Libya.

I would like to thank my friends including S. Schulze, U. Buttner, W. van Staden, and H. de Villiers for their companionship and support.

Contents

List of Figures

Chapter 1

Introduction

Superconducting materials form the foundation of commercial devices, which are capable of producing magnetic flux densities of about 200,000 times that of the earth, and of magnetometers used to detect fluxe smaller than 10^{-15} Tm^2.

1.1 History of Superconductivity

The phenomenon called superconductivity was discovered a century ago by Dutch professor, Heike Kamerlingh Onnes, at the University of Leiden. In 1911, Onnes discovered that at low temperatures (4.2 K) the electrical resistance of a mercury sample suddenly became immeasurably small. He continued this work by showing that Indium, Tin, and Lead became superconducting materials at 3.4, 3.7, and 7.2 K, respectively. Two years later, he received the Nobel prize for this work.

In the following decades many alloys and compounds exhibiting superconductivity were discovered, including Nb_3Sn (18.1 K) and niobium germanium (23.2 K), which held the record for the highest transition temperatures from 1954 to 1986 [1, 2].

In 1933, W.H. Meissner and R. Ochsenfeld discovered an important magnetic property of superconductors. They noted that at temperatures below a critical temperature, the magnetic field was expelled from superconductor specimens. Today, this phenomenon is known as the *Meissner effect*.

High temperature superconductors were first discovered in 1986. G. Bednorz and A. Müller made a ceramic superconductor from Lanthanum, Barium, Copper, and Oxygen (LaBaCuO) with a transition temperature of 30 K [2].

Their discovery triggered enormous growth in research in the field of superconducting materials. In 1987, P. M. Wu *et al* discovered $YBa_2Cu_3O_7$ (YBCO), which has a critical temperature of 92 K [3]. This was the first superconducting material of which the critical temperature was high enough to be cooled by liquid nitrogen, which is a cheaper and more convenient cryogenic refrigerant than liquid helium.

In the following years, related compounds based on copper oxides like $TlBa_2Ca_2Cu_3O_8$ with T_c = 130 K and $HgBa_2Ca_2Cu_3O_8$ with T_c = 164 K (at extremely high pressure) have been discovered. This temperature is only 19 K lower than the lowest recorded temperature reached on Earth [4]. Figure 1.1 shows the years of discovery of superconducting materials and their transition temperatures.

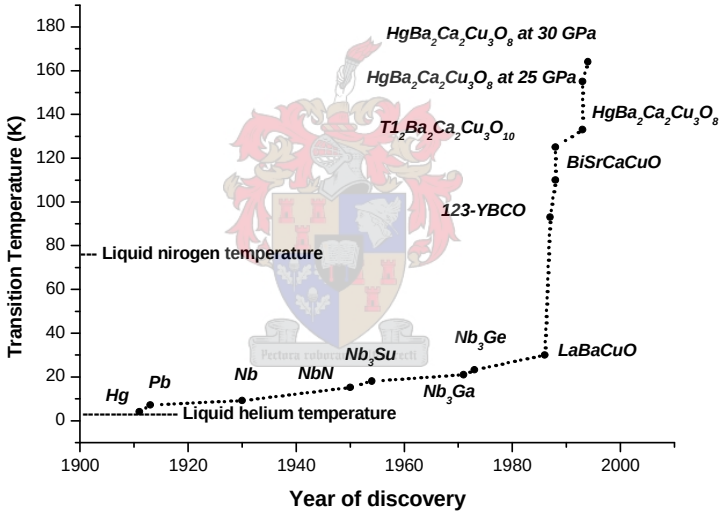

Figure 1.1: Superconducting transition temperature records through the years.

1.2 Basic Properties of Superconductors

Superconductive materials need an appropriate thermal and magnetic environment in order to exhibit their superconductive properties. The superconductor needs to be cooled below its critical temperature, T_c, or the superconducting state can not be present.
Superconductivity can be present in a magnetic field, but when the applied magnetic field exceeds a certain critical field, H_c, the superconductivity will cease to exist.

The current passing through superconductors has a boundary value known as the critical current, I_c. Above T_c, H_c or I_c the superconducting materials revert to their normal physical state.

The critical magnetic field H_c is a function of temperature and is given by the empirical formula

$$H_c(T) = H_{co}\left(1 - \left(\frac{T}{T_c}\right)^2\right) \qquad (1.2.1)$$

where H_{co} is the value of the critical field at T = 0 K [5].

One of the most fundamental properties of superconductors was discovered in 1933 by Meissner and Ochsenfeld. They observed that in the presence of a low magnetic field a cooled superconductor behaves as if the magnetic field within the specimens is zero (Figure 1.2). In other terms, the magnetic field is expelled by the superconductor.

This is caused by a surface current flowing in such a way that it creates an opposing magnetic field. When the external field is removed, the surface current remains due to the perfect conductivity. This phenomenon indicates that a superconductor is a perfect diamagnetic material [5, 6].

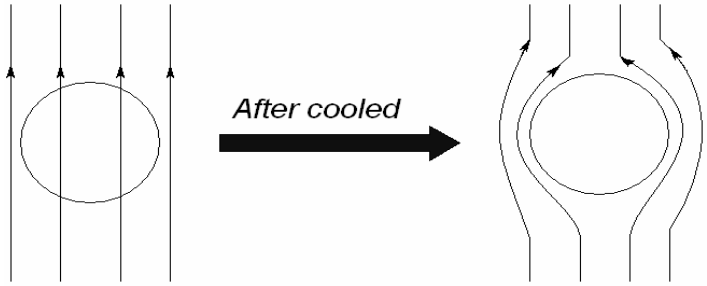

Figure 1.2: The Meissner effect in superconductors.

Generally, there are two categories of superconductors, called type *I* and type *II* superconductors. Type *I* superconductors are always pure metals, which have a low H_c and behave as perfect diamagnetic up to the point where the superconductivity is abruptly destroyed.

Type *II* superconductors are usually alloys or compounds. They have the capability to carry a large current density and they are diamagnetic in weak magnetic fields.
They show partial diamagnetism at an initial critical magnetic field, H_{c1}, and at a much higher second critical magnetic field, H_{c2}, their superconductivity disappears [2].

1.3 The Josephson Effect

In 1962, one of the most important discoveries in the field of superconductivity was predicted by B. D. Josephson. He proposed that a Cooper pair could tunnel through a thin insulating layer placed between two superconductors. Cooper pairs consist of two electrons that pair together to form superelectrons. Josephson predicted two effects known as the DC and AC Josephson effects.

The DC Josephson effect states that a current can flow through the junction when the voltage across it is zero [2], thus

$$V = 0 \quad \text{for} \quad i < I_c,$$

where I_c is the critical current of the junction.
The AC Josephson effect states that if a DC voltage, V is applied across the junction, an alternating current will flow through it. The ac current is expressed as

$$i = I_c \sin\left[\frac{2\pi V t}{\Phi_0} + j(0)\right] \tag{1.3.1}$$

where Φ_0 is one flux quantum ($\Phi_0 = 2.07\times10^{-15}\,Wb.$) and $\varphi(0)$ is an arbitrary phase constant.
The current will oscillate with a frequency of $2eV/h$, where h is Planck's constant.
A 1μV DC voltage across a junction therefore generates an alternating current with a frequency of 483.6 MHz.

There are several superconductive structures that exhibit the Josephson effect. One of these structures is the nanobridge.
The Josephson behaviour in nanobridges is caused by the Abrikosov vortices motion in the bridges. In the next section, the Abrikosov quantum vortex is introduced.

1.4 The Abrikosov Quantum Vortex

Two critical fields exist for a type *II* superconductor in an external magnetic field. In a magnetic field less than the lower critical field, H_{c1}, the superconductor is a perfect diamagnet exhibiting the Meissner effect. In an applied field greater than the upper critical field, H_{c2}, the superconductivity will be destroyed.

In a magnetic field between H_{c1} and H_{c2}, the magnetic flux is able to penetrate the superconductor in form of tubes called *vortices*. Abrikosov [7] observed the vortices in 1957. Each vortex has a normal core with a radius equal to the coherence length ξ.
The magnetic field inside the superconductor is strong at the normal cores of the vortices, and decreases in an approximately exponential manner far from the core. The value of the flux in each vortex was experimentally found to be a single flux quantum.
The vortex is held in its place in the superconductor by a pinning force F_p. However, when transport current J_{TR} is present, the Lorentz force $J_{TR} \times \Phi_o > F_p$ acts to unpin the vortex and induces the core of the vortex to move [5].

In the next chapter, the weak link behaviour in nanobridges as caused by coherent motion of Abrikosov quantum vortices across the superconducting bridge is described.

1.5 Applications of Josephson Junctions

Josephson junctions are the core of superconducting electronic devices; their unique *dc* and *ac* Josephson effects make them attractive in scientific and commercial applications. Josephson junctions are used in digital logic devices, such as the Complementary Output Switching Logic (COSL), which are the fastest voltage state logic [8, 9].

In the 1980s an important development in digital electronic field of superconductor applications has taken place, a new logic family, called Rapid Single Flux Quantum logic (RSFQ-logic) was introduced. Josephson junctions with their fascinating properties are the essential element in this new logic family which includes registers and latch circuits,

basic asynchronous components, such as pulse splitters and mergers and interface devices like DC to Single Flux Quantum (SFQ) converters [10].
Analog-to-digital converter circuits have thousands of junctions and operate at frequencies up to 11 GHz. RSFQ circuits are expected to operate at frequencies greater than 100 GHz [21].

Based on the AC Josephson effect, Josephson junctions have been used as radiation detectors and sources [6]. A set of junctions can act as a frequency source of the THz order. They are also used as the basis for a highly accurate voltage standard. With over 20,000 junctions, a 10 Volt standard Josephson junction array has been constructed [11].
The most widely used Josephson junction device is the Superconducting Quantum Interference Device (SQUID), which consists of a superconducting ring interrupted by one or two Josephson junctions. SQUID magnetometers and gradiometers are the most sensitive devices to detect magnetic flux. They have the ability to measure magnetic fields in the order of femto Tesla which makes this device a powerful tool in many application fields such as physical, geological, biological and medical applications [2, 6].

1.6 Aims and Overview of the Thesis

The aim of this thesis can essentially be divided in two parts. The first is to optimize the sidewall angle on photoresist lines with the Atomic Force Microscope (AFM). The angles of the photoresist sidewalls patterned on MgO substrates were not steep enough, which prevented the samples to be used in a successful argon ion milling process. It was attempted to cut these angles steeper using AFM in lithography mode. Diamond and silicon tips were used to manipulate the photoresist lines.

The second part is the fabrication of weak link junctions with the AFM. A small constriction on the superconducting YBCO line was created with a diamond tip to induce Josephson behaviour.
In Chapter 2 an overview of superconductivity is given. Theories based on electrodynamics, macroscopic and quantum mechanical properties of superconductivity are introduced. Based on these theories, aspects like the Meissner effect, flux quantization

and type *I* and type *II* superconductivity will be explained. The second section in Chapter 2 is described the Josephson junctions and weak links.

In Chapter 3, the fabrication steps of a nano-bridge on YBCO are illustrated. Information on the deposition of the YBCO film using Pulsed Laser Deposition (PLD), patterning and etching of the films, as well as AFM lithography are given. Chapter 4 illustrates the test and measurement setup. The experimental results are introduced and AFM images of the sidewall angles before and after lithography are shown. Conclusions and future recommendations are given in Chapter 5.

Chapter 2

Fundamental Theories of Superconductivity and Josephson Junctions

2.1 Introduction

After the discovery of the *Meissner effect* in 1933, numerous theories of superconductivity were developed. Some of these theories agreed well with experimental data, others less so.

This chapter gives an overview of theories and models of superconductivity that explain certain properties. The classical model incorporates zero electrical resistance and perfect diamagnetic properties of superconductors into electromagnetic constitutive relation equations.

This model is then expanded to include the macroscopic quantum nature of superconducting electrons. Finally, the Ginzburg-Landau theory is introduced where the superconducting electrons are described by an order parameter.

None of these theories can however, explain what is happening inside a superconductor at a microscopic level.

BCS theory is the only microscopic theory in the superconductivity field. The BCS theory was developed in 1957 by J. Bradeen, L. Cooper and J. Schrieffer. It demonstrates that electrons with opposite momenta and spins pair up into bound states called (Cooper pair) via the exchange of phonons.

BCS theory successfully explains the behaviour of the low temperature superconductors, for which the superconducting mechanism depends on a phonon-mediated attraction between electrons.

2.2 The Two-Fluid Model

All superconductors have to be cooled below its transition temperature in order to become superconductive. Thus the superconductor undergoes a thermodynamic change of state. Gorter and Casimir proposed the Two-Fluid model in 1934. It is based on the thermodynamic properties of the superconductors. According to the Two-Fluid model the total current flowing in a superconductor can be expressed as the sum of two "fluids": A normal current consisting of unpaired electrons and a supercurrent consisting of paired electrons. The total current is expressed as

$$J = J_n + J_s \tag{2.2.1}$$

where J_n and J_s are the normal current density and the supercurrent density respectively. At temperatures above the critical temperature T_c, the electrons contributing to conduction are normal electrons and there are no paired electrons involved. If the superconductor is cooled below its transition temperature T_c, the normal electrons begin to "condense" into pairs. At T = 0 K no unpaired electrons exist [2].

The density of superconducting electrons n_s at temperatures below T_c is

$$n_s = n_0\left(1 - \left(\frac{T}{T_c}\right)^4\right) \tag{2.2.2}$$

where n_0 is the density of superconducting electrons at $T = 0\,\mathrm{K}$.

2.3 The London Theory

In 1935, the brothers Fritz and Heintz London developed a phenomenological theory of superconductivity. The London Theory describes the perfect conductivity and perfect diamagnetic properties of superconductors with two equations.

The first London equation can be expressed as

$$E = \frac{\partial}{\partial t}(\Lambda J) \tag{2.3.1}$$

where Λ is the London coefficient which is defined as

$$\Lambda \equiv \frac{m^*}{n^*(q^*)^2}. \tag{2.3.2}$$

The star indicates that the quantity is associated with the superelectrons.

The first London equation shows that a perfect conductor develops a voltage across it when an alternating current is applied [5].

London predicted one of the two characteristic length scales in superconductivity theory called the *London penetration depth* λ, which is expressed as

$$\lambda = \sqrt{\frac{\Lambda}{\mu_o}} \tag{2.3.3}$$

where μ_o is the permeability of free space.

The London penetration depth is the extent to which a magnetic field penetrates into a superconductor. The value of the London penetration depth varies with temperature and can be related to its zero temperature value λ_0 by

$$\lambda(t) = \lambda_0 \left[1 - \left(\frac{T}{T_c} \right)^4 \right]^{-1/2}. \tag{2.3.4}$$

The second London equation can be written as

$$\nabla \times (\Lambda J) = -B. \tag{2.3.5}$$

The second London equation guarantees flux expulsion in superconductors, or in other words, it explains the experimentally shown Meissner effect.

In 1948, Fritz London proved that the London equations could be derived by treating the superelectron fluid as a quantum mechanical entity. From this the Macroscopic Quantum Model was derived, which is an extension of the classical model developed in order to explain the flux quantisation that could not be explained any other way [5].

2.4 The Macroscopic Quantum Model

"Superconductivity is an inherently quantum mechanical phenomenon that manifests itself on macroscopic scales", *Fritz London [5]*.

The hypothesis behind the Macroscopic Quantum Model of superconductivity is that there is a macroscopic quantum wave function $\psi(r,t)$, which describes the behaviour of the entire ensemble of superconducting electrons [5]. The wave function can be written in the form

$$\psi(r,t) = \sqrt{n^*(r,t)}e^{i\theta(r,t)} \tag{2.4.1}$$

where n^* is the density of superelectrons and θ represents the phase of the complex number.

Based on fundamental concepts of quantum mechanics, the macroscopic quantum current density in a superconductor in an electromagnetic field can be derived as

$$J_s = q^* n^*(r,t)\left(\frac{h}{m^*}\nabla\theta(r,t) - \frac{q^*}{m^*}A(r,t)\right). \tag{2.4.2}$$

Where $\hbar = h/2\pi$, A is the vector potential, q^* and m^* are the charge and the mass of the superelectrons.

Reintroducing the London coefficient Λ into (2.4.2) yields the supercurrent equation

$$\Lambda J_s = -\left(A(r,t) - \frac{h}{q^*}\nabla\theta(r,t)\right). \tag{2.4.3}$$

Both London equations can be derived from the supercurrent equation (2.4.3). By taking the curl of (2.4.3) the second London equation can be obtained

$$\nabla \times \left(\Lambda J_s \right) = -\nabla \times A = -B . \tag{2.4.4}$$

The partial derivative of (2.4.3) yields the first London equation

$$\frac{\partial}{\partial t}\left(\Lambda J_s \right) = E - \frac{1}{n^* q^*} \nabla \left(\frac{1}{2} \Lambda J_s^2 \right). \tag{2.4.5}$$

The Macroscopic Quantum Model is a powerful theory and very useful for understanding some of the fascinating properties of superconductors, such as the Josephson effect and flux quantization. Nevertheless, it does not explain the microscopic origin of superconductivity.

2.4.1 Flux Quantisation

Flux quantisation in superconductors is one of the features that can only be described by the Macroscopic Quantum Model.

Consider a superconductor with a hole in it as shown in Figure 2.1. Integrating the supercurrent of equation (2.4.3) on a closed contour around the hole yields

$$\oint_c \left(\Lambda J_s \right) dl + \oint_c A \, dl = \frac{h}{q^*} \oint_c \nabla \theta \, dl \tag{2.4.6}$$

Using Stoke's theorem, the vector potential *A* can be related to the magnetic flux density *B* as follows

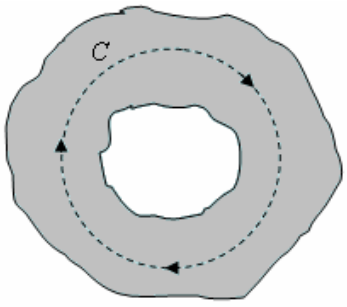

Figure 2.1: Cross-section of a hollow cylindrical superconductor.

$$\oint_c A \, dl = \int_s \left(\nabla \times A \right) ds = \int_s B \, ds \tag{2.4.7}$$

where s is the surface defined by the contour C.

Substituting (2.4.7) into (2.4.6) yields

$$\oint_c (\Lambda J_s)\, dl + \int_s B\, ds = \frac{h}{2\pi q^*} 2\pi n = n\Phi_0 \tag{2.4.8}$$

where Φ_0 is called a fluxon, or one flux quantum, which is the smallest amount of flux that can be included by the closed contour line and is given by

$$\Phi_o = \frac{h}{|q^*|} = 2.0679 \times 10^{-15} Wb. \tag{2.4.9}$$

Equation (2.4.8) shows that the magnetic flux in a closed superconducting loop can only change by multiples of the flux quantum Φ_o [5].

Flux quantization has been experimentally proven by R. Doll and M. Näbauer at the Walther-Meissner-Institute in Munich [12].

2.5 The Ginzburg-Landau Theory

In 1950 V. Ginzburg and L. Landau postulated the phenomenological theory of superconductivity that integrated the electrodynamical, quantum mechanical and thermodynamical properties of superconductors.

The Ginzburg-Landau theory introduced an effective wave function as an order parameter $\psi(r)$, such that the density of superconducting electrons is given by

$$n_s = |\Psi(r)|^2, \qquad \Psi(r) = \sqrt{n_s(r)}\, e^{j\theta(r)} \tag{2.5.1}$$

The *Ginzburg-Landau equation* and the *supercurrent equation* can then be written as

$$\alpha\Psi(r) + \beta|\Psi(r)|^2\Psi(r) + \frac{1}{2m^*}\left(\frac{\hbar}{i}\nabla - q^* A\right)^2 \Psi(r) = 0 \tag{2.5.2}$$

and

$$J_s = \frac{q^*}{m^*} Re\left\{\Psi^*\left(\frac{\hbar}{i}\nabla - q^* A\right)\Psi\right\} \tag{2.5.3}$$

where α and β are the Ginzburg-Landau coefficients depending on the temperature.

Equation (2.5.3) is the same supercurrent equation that was derived from the Macroscopic Quantum Model [5].

The Ginzburg-Landau theory introduces a second characteristic length ξ in the superconductivity theory, which is known as *coherence length* and is expressed as

$$\xi(t) = \frac{\hbar}{\sqrt{\left|2m^{*}\alpha\right|}} \tag{2.5.4}$$

Coherence length represents the size of the Cooper pair.

To write the Ginzburg-Landau equation in terms of the characteristic length, a dimensionless order parameter is introduced

$$f(r) = \frac{\Psi(r)}{\sqrt{n^{*}}} \tag{2.5.5}$$

The Ginzburg-Landau equation can then be written in terms of f as

$$\xi^{2}\left(\frac{\nabla}{i} + \frac{2\pi}{\Phi_{o}}A\right)^{2} f + \left|f\right|^{2} f - f = 0 \tag{2.5.6}$$

and the supercurrent equation in terms of f as

$$J_{s} = -\frac{\Phi_{0}}{2\pi A} Re\left\{ f^{*}\left(\frac{\nabla}{i} + \frac{2\pi}{\Phi_{0}}A\right) f \right\}. \tag{2.5.7}$$

The Ginzburg-Landau theory was not widely accepted outside the Soviet Union, but this changed in 1959, when L. P. Gorkov showed that at temperatures near the critical temperature the Ginzburg-Landau theory could be derived from the Microscopic BCS theory. Since then the Ginzburg-Landau theory became a powerful tool for the understanding of superconductivity.

Based on the GL theory, Abrikosov [7] predicted that, when $K = \frac{\lambda}{\xi} < \frac{1}{\sqrt{2}}$ the superconductor expels a magnetic field and it is called a type *I* superconductor. When $K = \frac{\lambda}{\xi} > \frac{1}{\sqrt{2}}$ the superconductor accommodates vertices to form a mixed state, which is known as type *II* superconductor. Soon after, Abrikosov prediction was demonstrated practically [14].

2.6 The Josephson Junction

Josephson Junctions are essential components in digital superconductor devices. There are two types of superconductor structures where Josephson effects can take place: A superconductor insulator superconductor (SIS) structure and a weak link. An SIS structure is known as a *tunnel junction*.

The weak link is demonstrated in several stuctures, such as a superconductor normal metal superconductor (SNS) structure or proximity effect junction, point contacts, microbridges and nanobridges [15].

In this section, the theory of Josephson Junctions is given, and a micobridge weak link in low temperature superconductors (LTS) and a nanobridge weak link in high temperature superconductors (HTS) are illustrated.

2.6.1 Tunnel Junction

B. Josephson predicted that it would be possible for Cooper pairs to tunnel through a thin barrier placed between two superconductors. He used the BCS theory to calculate the probability of a Cooper pair tunnelling through the barrier [16].

A tunnelling junction consists of two superconductors separated by a thin isolating layer. The wave function of the Cooper pairs from each superconductor penetrates the junction, and if the isolating layer is thin enough, the wave functions interact. This effect is called coupling. When the phases of wave functions are locked, the Cooper pairs can pass through the isolating layer from one connector to other without energy loss. Cooper pair tunnelling can occur without applying a voltage across the junction [17].

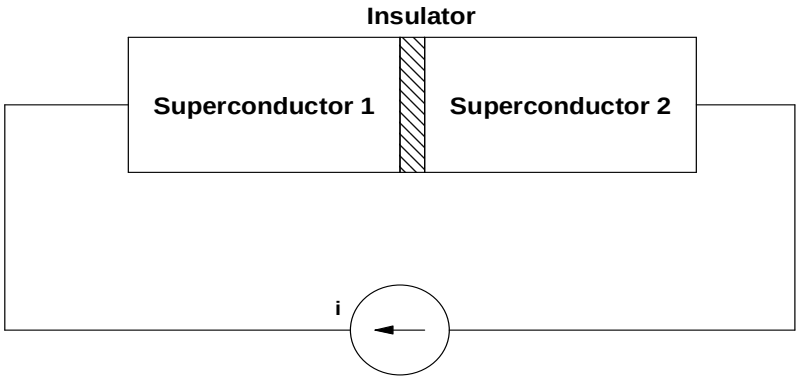

Figure 2.2: A tunnel junction with a current source

2.6.1.1 The Basic Josephson Junction

The behaviour of the basic lumped junction can be described mathematically as follows: From the Macroscopic Quantum Model the supercurrent equation, describing the current density of superelectrons in a single piece of metal, can be written as

$$J_s(r,t) = -\frac{1}{\Lambda}\left[A(r,t) + \frac{\Phi_0}{2\pi}\nabla\theta(r,t)\right]. \tag{2.6.1}$$

The energy-phase relationship can be written as

$$\frac{\partial}{\partial t}\theta(r,t) = -\frac{1}{h}\left[\frac{\Lambda J_s^2}{2n^*} + q^*\varphi(r,t)\right]. \tag{2.6.2}$$

This shows how the phase of the wave function changes in time as the energy of the superelectrons changes.

Assuming the current density is uniform across the junction and the magnetic vector potential is zero, the supercurrent density in the system can be written as

$$J_s = J_c \sin(\theta_1 - \theta_2) \tag{2.6.3}$$

where J_c is known as the critical current density of the junction. Its magnitude is given by

$$J_c = \frac{e\hbar\sqrt{n_1\, n_2}}{2m\,\zeta\, \sinh(2a/\zeta)} \tag{2.6.4}$$

where n_1 and n_2 are the electron densities on the two sides of the insulator, a is the thickness of the insulator and ζ is known as the decay length [5].

The generalised current-phase relation can be written as

$$J_s(r,t) = J_c \sin \varphi(y,z,t) \tag{2.6.5}$$

where φ is the gauge-invariant phase difference and is given by

$$J(y,z,t) = \theta_1(y,z,t) - \theta_2(y,z,t) - \frac{2\pi}{\Phi_0}\int_1^2 A(r,t)\ dl\,. \tag{2.6.6}$$

From the energy-phase relation (2.6.2) and the gauge-invariant phase difference (2.6.6) the following voltage-phase relation can be derived:

$$\frac{\partial \varphi(y,z,t)}{\partial t} = \frac{2\pi}{\Phi_0}\int_1^2 E(r,t)\ dl\,. \tag{2.6.7}$$

The term $\int_1^2 E(r,t)\ dl$ is the voltage across the junction (v).

Therefore, the two relationships to describe the lumped basic Josephson junction are the Josephson current-phase relationship,

$$i = I_c \sin \varphi(t), \tag{2.6.8}$$

and the Josephson voltage-phase relationship,

$$v = \frac{\Phi_0}{2\pi}\frac{\partial \varphi}{\partial t}\,. \tag{2.6.9}$$

2.6.1.2 Generalized Josephson Junctions

In a basic Josephson junction the current through the junction is always restricted to be less than the critical current.

When the current exceeds the critical current the generalized Josephson junction model is used to provide a complete description of the Josephson junction's behaviour. Two additional parallel channels must be added to the basic lumped Josepson junction, namely a resistive channel and capacitive channel.

According to the two fluid model, normal electrons will exist in the superconductor at temperatures above T = 0 K. These normal electrons tunnel through the barrier so that a resistive part appears even at voltages less than the gap voltage $V_g = 2\Delta/e$ where 2Δ is the energy required to break up a Cooper pair. The normal conductance channel can be generalized to give

$$G(v) = \begin{cases} \dfrac{1}{R_{sg}(T)} & if\ |v| < 2\Delta(T)/e \\ \dfrac{1}{R_N} & otherwise \end{cases} \tag{2.6.10}$$

where R_{sg} is called subgap resistance which is a function of temperature [5].

Above the gap voltage all the Cooper pairs become unbounded single electrons and a normal resistance is observed due to the tunnelling of normal electrons through the barrier in the Josephson junction.

The product of the normal resistance, R_N, and the critical current, I_c, is an important junction parameter, given as

$$I_c R_N = \frac{\pi\ \Delta(T)}{2e}. \tag{2.6.11}$$

The junction capacitance is calculated in the same way as for a parallel plate capacitor. The insulator is considered as an ideal insulator with a permittivity ε, cross section *A*, and thickness d. The capacitance is thus given by

$$C = \frac{\varepsilon A}{d}. \tag{2.6.12}$$

This model is called the non-linear resistively shunted junction (NRSJ) model.

If the non-linear conductance is replaced by a constant resistance $G = 1/R_N$, then the model is called a resistively shunted junction (RSJ).

The RSJ model is widely used to analyse the junction characteristics. Figure 2.3 illustrates both NRSJ and RSJ models.

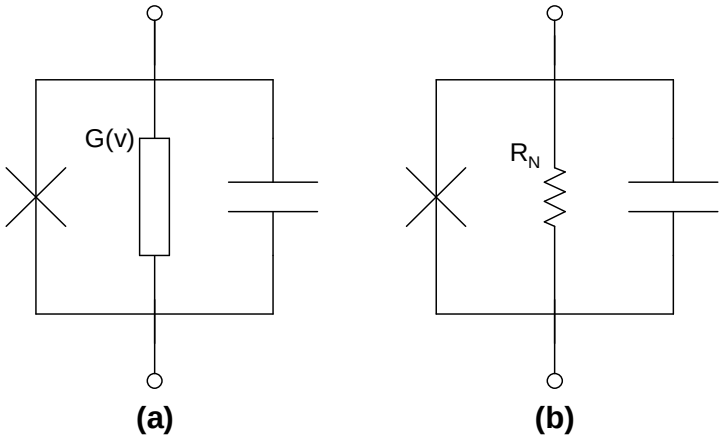

Figure 2.3: Generalized Josephson junction (a) NRSJ and (b) RSJ models.

If a current source is connected across the generalized Josephson junction, the total current can be found using Kirchhoff's current law and can be written as

$$i = I_c \sin\phi + C\frac{dv}{dt} + \frac{v}{R}. \tag{2.6.13}$$

The voltage across the generalized junction is the same voltage as in (2.6.9), and by substituting (2.6.9) into (2.6.12), we obtain the second order differential equation for the current through the junction

$$i = I_c \sin\phi + \frac{1}{R}\frac{\Phi_0}{2\pi}\frac{d\varphi}{dt} + C\frac{\Phi_0}{2\pi}\frac{d^2\varphi}{dt^2}. \tag{2.6.14}$$

The current equation (2.6.14) can be written as a dimensionless equation

$$\frac{i}{I_c} = \sin\phi + \frac{d\varphi}{d\tau'} + \beta_c \frac{d^2\varphi}{d(\tau')^2} \tag{2.6.15}$$

where

$$\beta_c = \frac{RC}{\tau_J}, \tag{2.6.16}$$

$$\tau_J = \frac{\Phi_0}{2\pi I_c R} \tag{2.6.17}$$

and

$$\tau' = \frac{t}{\tau_J}. \tag{2.6.18}$$

The parameter β_c is called the Stewart-McCumber parameter. It is a measure of the influence of the junction capacitance.

If the applied DC current to the junction is increased from zero, there will be no voltage across the junction until the critical current is exceeded. Just above the critical current the value of the voltage across the junction increases from zero to a finite voltage (subgap voltage). Hereafter, the voltage is related to the current by $V = i R_N$.

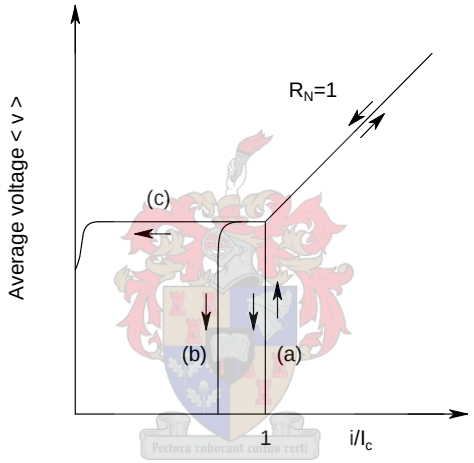

Figure 2.4: Average voltage versus current for (a) $\beta_c \ll 1$ **(b)** $\beta_c \approx 1$ **and (c)** $\beta_c \gg 1$.

If the current is decreased again, it follows the same path in reverse until the critical current is reached. When the current is reduced below I_c, the path is determined by the value of β_c which is proportional to the junction capacitance.

For $\beta_c \ll 1$, the voltage follows the same path as it did when the current was increased.

For $\beta_c \gg 1$, a finite voltage remains in the junction until the current nearly reaches zero, where it shows a significant hysteresis.

Figure 2.4 displays the characteristic curve of the current versus the average DC voltage. The flow of a supercurrent without any voltage drop was observed experimentally by Anderson and Rowell [18].

2.6.2 The Weak Link

The Josephson effect is not limited to classic tunnel junctions. It can take place in any kind of inhomogeneous structure where the superconductivity is suppressed [15]. Different superconducting structures called weak links, exhibit a similar Josephson effect when the dimensions of such weak links are sufficiently small.

The term "weak link" describes the conducting junction between two superconducting electrodes. The critical current through the junction is less than that in the electrode [19]. The classic tunnel junction is limited onto the SIS structure, but a weak link is found in many structures such as a SNS junction, a microbridge, an ion-implanted bridge, and a point contact, as illustrated in Figure 2.5.

The main advantage of these structures over tunnel junctions is that the junction capacitance is lower [15].

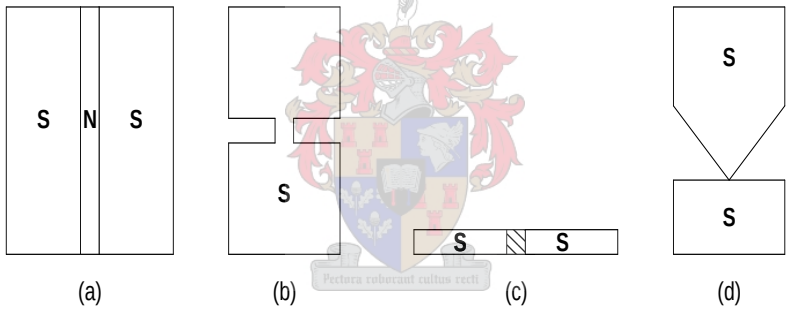

Figure 2.5: Different types of structures where the Josephson effect can take place. (a) SNS junction (b) microbridge (c) ion-implanted bridge (d) point contact.

The Josephson effect was observed in weak link structures "non-tunnel conductivity" in 1964 by several researchers. The use of weak link structures for practical purposes, however, only began in 1966.

In Figure 2.5a, a layer of a normal metal is placed between two superconducting electrodes. Such a structure is called a "S-N-S sandwich" junction.

When a normal metal and a superconducting metal are brought into good electrical contact, some Cooper pairs will penetrate into the normal metal from the superconductor causing a finite supercurrent to flow through such a junction. This is known as the *proximity effect*.

The microbridge Figure 2.5b is created by narrowing a small section in a continuous superconducting strip. This small section reduces the critical current of the superconducting strip so that the critical current at that point is much smaller than the critical current of the superconducting strip, thereby causing the superconductor to convert into a normal conductive state [19].

A structure closely resembling the sandwich structure is the in ion-implanted bridges of Figure 2.5c. A section with a low critical current is created in a narrow strip of the superconducting film by implantation of ions into this region.

A more complicated geometry of a weak link is created in a point contact junction shown in Figure 2.5d. The electrical contact is created by two weakly touching superconductive electrodes. When a pressure is applied to the electrodes, the oxide layer is interrupted at many places, thereby forming several metallic connections between the electrodes. The significant disadvantage of the point contact junction lies in its poorly defined geometry and its irreproducibility [15].

2.6.2.1 The Josephson Microbridge

The weak link in microbridge is explained based on GL theory, from which the relationship between the current density and phase difference across the weak link can be derived.

This relationship is similar to that describing a classic tunnel Josephson junction.

Consider a superconductor with the geometry displayed in Figure 2.6. The constricted region has the length l that is much smaller than the coherence length ξ [5].

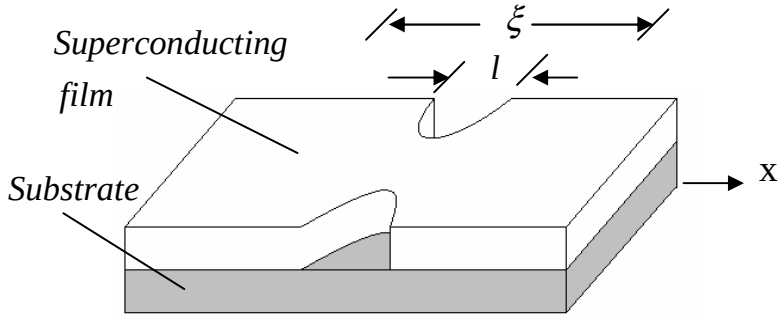

Figure 2.6: Superconducting thin film with a geometrical restriction with the characteristic length $l \ll \xi$.

To determine the relation between the current density and the phase difference over the weak link a case is considered where the vector potential is zero. The GL equation (2.5.6) then becomes

$$\xi^2 \nabla^2 f + f\left(1 - |f|^2\right) = 0. \tag{2.6.19}$$

Since f is of the order of unity and $l \ll \xi$, the derivative term is of the order

$$\xi^2 \nabla^2 f \sim \frac{\xi^2}{l^2} f \gg 1. \tag{2.6.20}$$

The derivative term is much larger than the other terms, therefore, the dimensionless order parameter ξ is governed by the Laplace equation

$$\xi^2 \nabla^2 f = 0. \tag{2.6.21}$$

Far from the constricted region the order parameter can be assumed to be constant,

$$f(\mathrm{r}) = \begin{cases} |f_1| e^{i\theta_1} & as\ x \to -\infty \\ |f_2| e^{i\theta_2} & as\ x \to +\infty \end{cases} \tag{2.6.22}$$

where f_1, f_2, θ_1, and θ_2 are position independent. x is the distance from the centre of the microbridge.

The normal component of the supercurrent must be zero at the surface of the microbridge, thus the boundary condition will be satisfied if $n \cdot \nabla f = 0$ along the surface of the microbridge and n is a unit vector normal to the surface.

If the real function g(r) satisfies the Laplace equation

$$\nabla^2 g(\mathrm{r}) = 0 \tag{2.6.23}$$

and satisfies the boundary conditions

$$g(\mathrm{r}) = \begin{cases} 1 & x \to -\infty \\ 0 & x \to +\infty \end{cases} \tag{2.6.24}$$

and

$$n \cdot \nabla \mathrm{g} = 0, \tag{2.6.25}$$

$f(\mathrm{r})$ can be expressed in terms of $g(\mathrm{r})$ as

$$f(\mathrm{r}) = |f_1| e^{i\theta_1}\ g(\mathrm{r}) + |f_2| e^{i\theta_2} \left[1 - g(\mathrm{r})\right] \tag{2.6.26}$$

With this expression the supercurrent through the microbridge (eq. 2.5.7) can be calculated as

$$J_s = J_c(\mathrm{r})\sin(\theta_1 - \theta_2) \tag{2.6.27}$$

where

$$J_c = \frac{\Phi_0 |f_1||f_2|}{2\pi\Lambda}\nabla g\,. \tag{2.6.28}$$

The supercurrent is of the same form as for classic tunnel Josephson junction, which shows that the microbridge will exhibit the Josephson effect if the order parameter is made to change over a distance of the coherence length. As the characteristic length, l, becomes larger than the coherence length, the structure will act as a bulk superconductor.

2.6.3 High Critical Temperature Josephson Junctions

Fabrication of a Josephson junction with properties such as nonhysteretic I-V characteristic, a high I_cR_N product, controllable and reproducible parameters (I_c, R_N, C), high stability, and low 1/f noise in low temperature superconductors is a simple task. Unfortunately, this is not the same in high temperature superconductors (HTS). The preparation of SIS tunnel junction in HTS is extremely difficult.

The preparation is complicated by the requirement of a full epitaxial layer structure, the short coherence length of the Cooper pairs and the sensitivity of the HTS to structural and chemical changes (surface instability).

Basically there are two kinds of natural Josephson junctions that manifest in high temperature superconductors: Intrinsic Josephson junctions and grain boundary junctions. Intrinsic Josephson junctions occur naturally between successive CuO_2 layers. They have been observed in both single crystals and thin films of highly anisotropic materials.

The grain boundary junctions occur when two adjacent grains are not perfectly aligned [20].

There are various types of HTS Josephson junctions, which can be fabricated by using artificial grain boundaries. Figure 2.7 illustrates some HTS Josephson junctions:

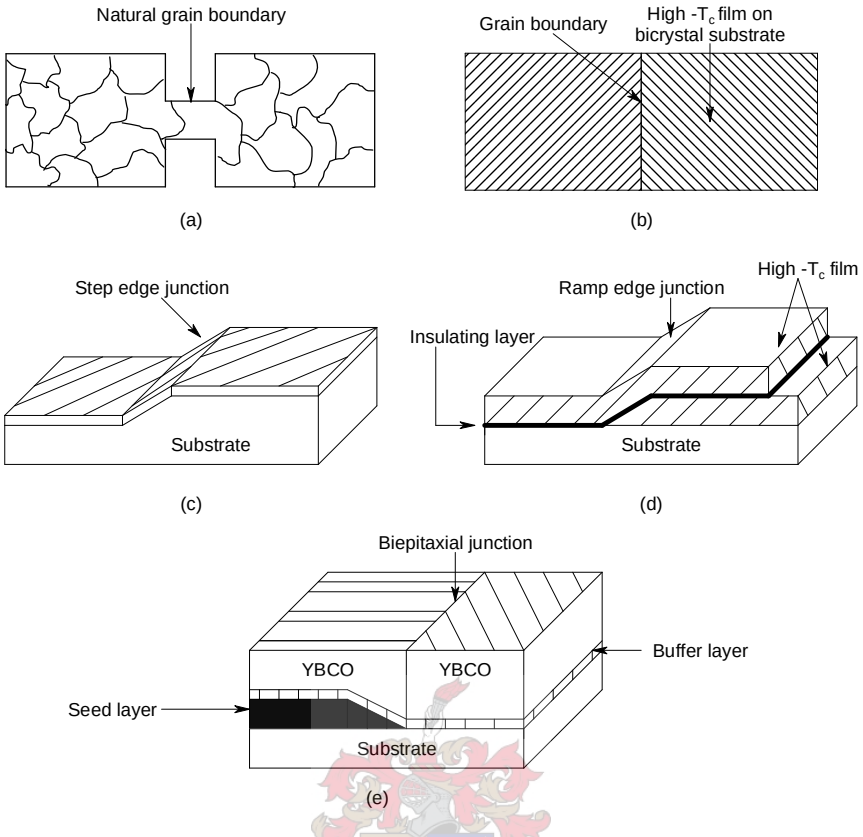

Figure 2.7: Various types of high –T_c Josephson junctions: (a) natural grain boundary, (b) bicrystal junction, (c) step-edge junction, (d) multilayer ramp-edge junction and (e) biepitaxial junction [20].

The earliest natural grain boundary junctions were produced by fabricating a thin section on a superconductor polycrystalline film. The thin section is grown on one or more naturally occurring grain boundaries.

These grains are randomly orientated and meet at grain boundaries with varying misorientation angles, as illustrated in Figure 2.7a.

It has been possible to use natural grain boundary (NGB) junctions in rf-SQUIDs, because only one junction is required. The fabrication of a NGB dc-SQUID however has not been very reproducible because the characteristics of NGB junctions vary from one grain boundary to another [21].

A bicrystal grain boundary junction (Figure 2.7b) is fabricated by growing an epitaxial HTS film on a bicrystal substrate. The bicrystal substrate is made by gluing two single-crystal substrates with different grain orientations together.

A grain boundary forms accordingly in the HTS film at the interface. The critical current density decreases sharply across the interface. This exponential degradation of the critical current is a function of the misalignment angle between the two substrates [20].

Figure 2.7c displays a HTS step edge junction. The junction is formed by growing a thin HTS epitaxial film on substrate with a step. A sharp step on a single-crystal substrate is created by photolithography or electron beam lithography and ion-beam-milling.
The transport properties of the junction greatly depend on the film thickness and the step profile, such as height and step angle [21]. Step-edge junctions can be manufactured on a variety of large-area substrates and placed anywhere on the substrate. This is, however, more complicated to manufacture than a bicrystal junction.

Ramp edge junctions are fabricated in a multi-layer process. A HTS layer is deposited onto a substrate, and then a ramp edge is created on this layer by using lithography and an etching process. A thin insulating layer and second HTS thin layer are then deposited on the ramp edge. These junctions are the most promising junction type for HTS digital circuits, because their multi thin layer process makes it easy to induce a ground plane. A ramp edge junction is shown in Figure 2.7d.

Another type of HTS Josephson junction named biepitaxial grain boundary junction is illustrated in Figure 2.7e. Here, a thin “seed layer” is deposited over a part of the substrate to produce a new surface with a different growth pattern.
The subsequently deposited epitaxial buffer layer as well as the epitaxial HTS thin film grow in two different orientations, separated by a certain angle grain boundary [21].

Gross *et al* [20] classified HTS Josephson junctions into three basic types: Josephson junctions with intrinsic interfaces, which are naturally formed junctions. Junctions such as the biepitaxial, the step edge and the bicrystal grain boundary all fall in this class. The second class is called “Josephson junctions with extrinsic interfaces”, such as the ramp edge junction. The third class is called “Josephson junctions without an interface”. These junctions are created by weakened superconductive structures. Constriction type junctions, such as nanobridges are an example. The weak coupling is achieved by

degrading the superconducting properties with focused electron or ion beam irradiation [29].

The detailed transport mechanism for most HTS Josephson junctions has not yet been identified, due to the complicated nature of both interface layers and barrier materials.

2.6.4 Nanobridges as Weak Links

Superconducting thin film nanobridges have shown the Josephson effect caused by periodic vortex motion across the bridge when their width and length are less than a few times the coherence length ξ [22, 19]. However, they also show Josephson behaviour when the size of the bridge is smaller than, or comparable to the effective London penetration length λ_{eff} [23, 24], where $\lambda_{eff} = \lambda_L \coth\left(d / 2\lambda_L\right) \approx 2\lambda / d$, and where d is the thickness of the film. The forces acting on the vortices in a nanobridge are schematically illustrated in Figure 2.8. A transport current that passes through the bridge induces a magnetic field across it.

The magnetic field can penetrate into the superconducting thin film in the form of Abrikosov vortices if the field is larger than the lower critical field H_{c1}.

Two vortices with opposite orientation will be created simultaneously at the edge of the bridge. The pinning force F_{pin} at the edges will act on the vortices. When the transport current is increased the Lorentz force F_L acting on the vortex will overcome this pinning force.

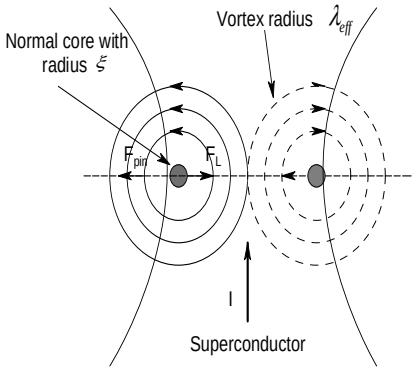

Figure 2.8: Forces acting on two Abrikosov vortices in a superconducting thin film nanobridge.

If the transport current density exceeds the critical current density of the bridge, these vortex-antivortex pairs are moved perpendicular to the direction of the driving current toward the center of the bridge, where they finally annihilate [25].
The Abrikosov vortices motion can be coherent due to the strong interaction between the vortices, causing periodical oscillations in the electrical and magnetic field emitted by the bridge.

Several publications on low temperature superconductor (LTS) SQUIDs based on nanobridges were published [26, 27]. Nanobridges have also been used in high temperature superconductor devices such as superconducting flux-flow transistors [28], and SQUIDs. D. H. Blank *et al* were the first to demonstrated HTS SQUIDs based upon nanobridges [29, 30].

2.6.5 Noise in Josephson Junctions

Thermal noise and flicker noise are the most common in HTS Josephson junctions and SQUIDs.
Thermal noise or "Nyquist noise" is produced by the random motion of charge carriers in the conducting medium. Thermal noise has a flat "white noise" spectrum at intermediate frequencies. It depends on temperature since the charge carriers are thermally excited.
Flux noise in a SQUID loop inductance is caused by the thermal noise created by the current in the resistive channel of the junction [31].
Flicker noise, also known as $1/f$ noise, occurs at low frequencies and its magnitude is inversely proportional to the operating frequency. It is not fully understood in LTS and HTS Josephson junctions. Flicker noise has no effects on digital devices that operate at a GHz range.

2.7 Summary

In this Chapter the classical models of superconductivity, including the two-fluid model and the first and second London equations were introduced. The classical model explains the thermodynamic properties, perfect conductivity and diamagnetism of

superconductors. The Macroscopic Quantum Model was described and based on this model the flux quantization was explained.

The Ginzburg-Landau theory was described and the effective wave function was introduced. The second characteristic length (*coherence length)* in superconductivity field was introduced.
The Abrikosov used the GL theory to distinguish between type *I* and type *II* superconductors.
The Josephson junction and weak link effect were explained in the second part of this chapter. LTS and HTS Josephson junctions were described, and illustrated with schematic diagrams.

Based on the GL theory the weak link effect in a microbridge was explained, where the relationship between the current density and phase difference across the weak link was derived. The GL theory can not be applied on HTS material due to the short coherence length. The Josephson behaviour in nanobridges, as caused by a coherent motion of Abrikosov quantum vortices, was described at the end of this chapter.

Chapter 3

The Fabrication Process

This chapter discusses the steps involved in the HTS Josephson junction fabrication process. Steeping the angle of sidewall on photoresist lines was done by photolithography and subsequent nanolithography with AFM. The steps used to fabricate nanobridge junctions are explained. The entire process of nanobridge fabrication can be summarized as follows:

- A thin YBCO film is deposited on a clean Magnesium Oxide (MgO) substrate with Pulsed Laser Deposition (PLD).
- The photolithography is done on the deposited films in order to pattern the YBCO lines onto the substrate.
- The films are wet etched and nanobridges are manufactured by constricting the YBCO line widths with AFM lithography.
- Wire bonding is the last step in the process.

3.1 Photolithography

Photolithography is a method to print an electrical circuit layout onto a substrate. The substrate is first coated with photoresist which is an organic polymer, of which the solubility changes drastically in specific solvents as a result of exposure to ultraviolet (UV) radiation. Exposing the resist to UV light causes it to soften in the case of positive resist, or harden for negative resist. Subsequently the sample is developed in a chemical solution, which removes the soft parts of the resist. Each part of the process is described below.

3.1.1 Coating the Substrate with Photoresist

First the substrate must be well cleaned to remove any surface contamination and to improve the adhesion of the photoresist on the substrate. The optimum steps to clean the substrate are:

- Soaking in acetone in an ultrasonic bath (5 min).
- Soaking in methanol in an ultrasonic bath (5 min)
- Rinsing with isopropyl alcohol and with deionised (DI) water, and drying in nitrogen gas.
-

Shipley S1818 positive photoresist was used in this project.

After cleaning the sample, it is placed in a spinning machine and covered with photoresist. It is important to ensure that the entire surface of the substrate is covered.

The sample is spun at 4600 rpm for 60s. The spin speed, time of spinning, and the viscosity of the resist are important factors influencing the final resist thickness.

3.1.2 Pre-exposure Bake

The coated substrates are baked on a hot plate at 115^{o}C for 2 to 5 minutes [32]. A pre-exposure bake or soft bake is used to evaporate the solvent from the resist. It is a critical step because the soft bake affects the photoresist properties. Baking for a short time will lead to insufficient removal of the solvent of the resist, which will affect the resist profile. Over baking can destroy the photoactive compound of the resist and reduce its sensitivity.

3.1.3 Exposure

After the coated substrate is baked and cooled down to room temperature, it is placed under a chrome contact mask in a mask aligner. The mask is aligned with the substrate by micrometre adjustment screws in the alignment machine.

The alignment can be verified by a microscope. The substrate is held down by vacuum and then lifted up until it is in physical contact with the mask. The light source in the exposure machine illuminates through the mask onto the substrate.

The exposure time depends on several factors, such as the resist film thickness, and the UV light intensity. An exposure time of 15s was used in all the experiments described here [31].

The sample is immersed in the MF320 developer immediately after exposure for 45 seconds. The development is stopped by dipping the sample in DI water.

3.1.4 Hard Bake

Hard bake is used to improve the adhesion between the resist and the substrate. It is used to increase the photoresist's wet and dry etch resistance by hardening it [33].

The samples are hard baked on the hot plate for 20 to 40 minutes at 95^{o}C. In both the soft and hard bake the baking temperature should not exceed 130^{o}C, which is the glass transition temperature of the photoresist.

With these steps, photoresist lines with different sidewall angles are manufactured onto the substrate. The sidewall angle in the resist can be optimized by controlling factors, such as the baking, exposure and developing conditions.

Each photoresist is designed to have high contrast over a particular wavelength region. If the resist is exposed to light that has an inappropriate wavelength, the sidewall profile will be sloped, because of the higher absorption in the resist. A sidewall slope is, however, always observed, even at the appropriate wavelength.

L. H. Snetler [35] suggested that the sidewall angle in the resist obtained in the argon ion mill process was not steep enough. AFM was therefore used to increase the sidewall angle of the resist.

Figure 3.2 shows AFM images of two photoresist samples after photolithography. It displays the sidewall angles and the height of the resist on the substrate.

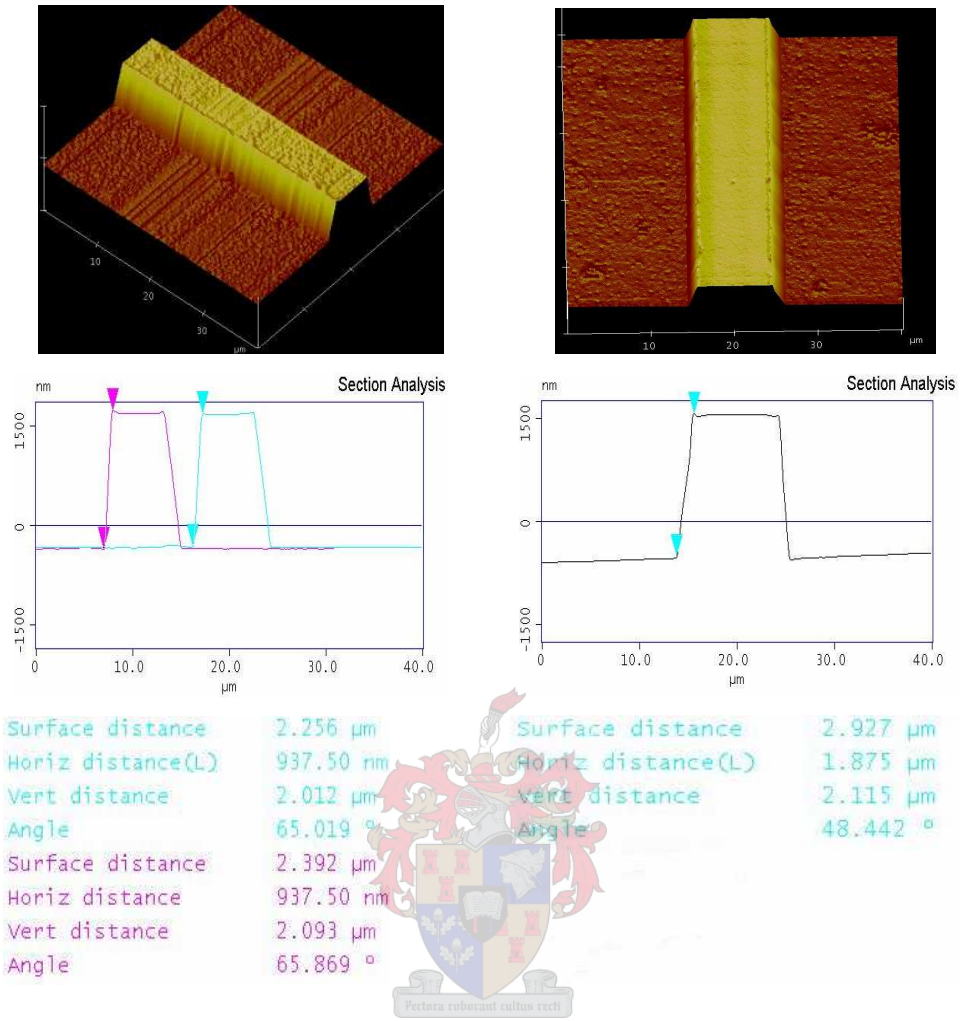

Figure 3.1: AFM images of two different samples with different sidewall angles after photolithography.

3.2 Atomic Force Microscopy

AFM is a member of the scanning probe microscopes (SPM) family. It was invented in 1986 by G. Binning *et al* [36].

AFM is used to image surface topography and it can measure electrical, chemical, and mechanical properties of conductive and nonconductive materials on a molecular scale. It detects the forces interacting between the sharp tip and the sample surfaces from which e.g. a topography profile can be derived [37].

3.2.1 Principle of Operation

The contact mode operation of AFM is illustrated in Figure 3.3.

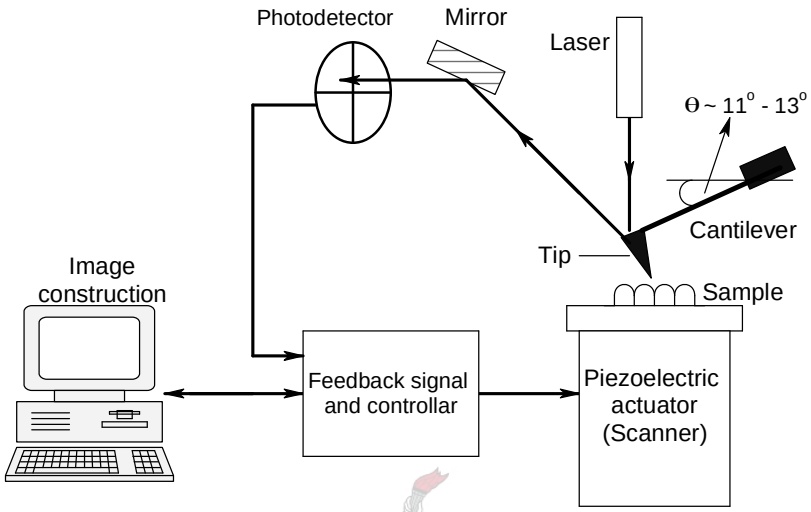

Figure 3.2: Block diagram of the essential compounds of an AFM in contact mode operation.

In contact mode, the tip touches the sample surface, as it is raster scanned across the surface. A laser beam is focused on the back of the cantilever and reflected into a mirror, where it is reflected again onto a multi-segmented photodetector. Features with varying height on the sample deflect the cantilever and with it the laser beam. This deflection results in a different reading at the photodetector [37]. The output of the photodetector is fed into the controller to maintain a constant value of force by means of a piezoelectric actuator. The voltage necessary to maintain a constant force on each scan point in the image results in a topographical image with nanometer resolution.

The tips are manufactured from silicon (Si). The tip is mounted at the end of a flexible micro-cantilever, which bends easily in response to the interacting forces between the tip and the sample surface. Figure 3.4 shows scanning electron microscope (SEM) images of AFM cantilevers and tips.

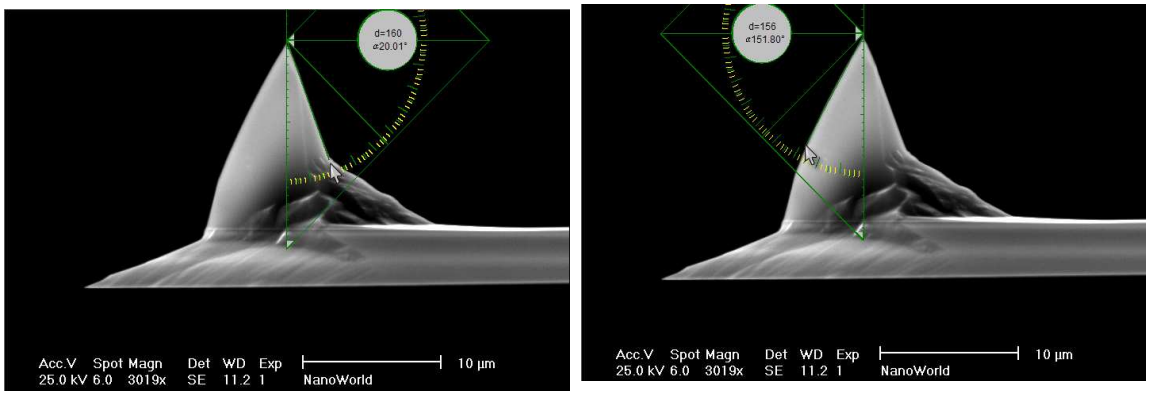

(a) (b)

Figure 3.3: SEM images of AFM cantilever and tip, (a) point-probe back angle and (b) point-probe front angle.

3.2.2 AFM Operating Modes

The AFM can work in three types of modes: contact, non-contact, and tapping mode. Each mode has its advantages, which depend on the application and the sample type and surface. In this study, the contact and tapping mode were applied

3.2.2.1 Contact Mode

In contact mode, the tip makes soft physical contact with the sample surface. As the scanner traces the tip across the sample surface, the cantilever is deflected by the contact force to accommodate changes in topography. The cantilever deflection is maintained at constant level by the feedback control system, by applying a voltage to the piezoelectric actuator. The voltage causes the scanner to move up or down in vertical direction with a distance proportional to the voltage magnitude. The applied voltage can be converted into height information to create images [38].

Frictional force is the main disadvantage of the contact mode, as it may cause damage to the sample.

3.2.2.2 Tapping Mode

To overcome the frictional force problem, tapping mode is used to image the surfaces. The tip is oscillated above the sample and contacts the sample surface once in each oscillation cycle. In tapping mode the tip and the sample surface are separated by a small distance. The amplitude and the resonance frequency of the cantilever's oscillation changes as the tip-sample distance changes.

As the probe is scanned over the samples surface, topography may change, and this change results in a change in the oscillation amplitude or in the resonance frequency, which is detected by the control unit. The system then applies a voltage to the piezoelectric actuator to maintain the set amplitude or resonance frequency. Due to the larger distance between the probe and sample, the resolution is not as good as in contact mode [39]. More information about AFM can be found in [40].

Figure 3.5 shows the AFM instrument at Stellenbosch University at the Polymer Science Institute, which was used for the work in this project.

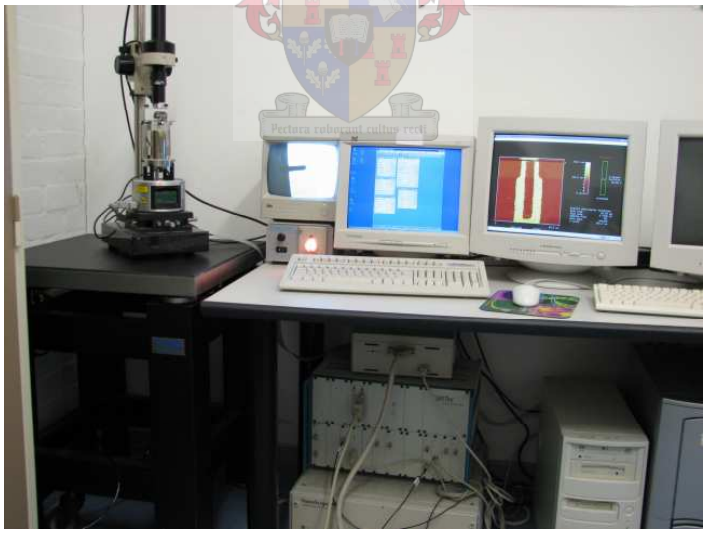

Figure 3.4: AFM at the University of Stellenbosch. A SQUID image is displayed on the third monitor.

In this project, contact and tapping mode were used to study the roughness of the sample surface (both photoresist and YBCO deposited samples), and to determine the sidewall angles of the resist lines. AFM was also used to increase these angles.

The additional lithography program allows the microscope to be used to inscribe lines on the material surfaces by using a sharp tip as an electrical or mechanical tool.

Nanolithography [41] can be performed in both contact and tapping mode. Although silicon tips can be used for lithography, diamond tips are preferable to use for hard surfaces. The diamond tip is a silicon tip coated with a diamond layer, which makes it much harder than the silicon tip.

Nanolithography was used to improve the sidewall angle in photoresist lines. First, the sample was imaged to determine the line dimensions, and then lithography was performed. The program starts by moving the tip to the center of the image, and then shifting it by a pre-defined distance to the starting point, where it approaches the sample surface at the side of the resist line. The tip moves parallel to the line over several μm. This results in a steeper sidewall angle where the AFM tip manipulates the resin. The sidewall angle is measured by scanning across the photoresist line.

An example of the source code used is shown in Appendix A. Figure 3.6 shows an example of nanolithography on a $60\times60\,\mu m^2$ resist coated substrate.

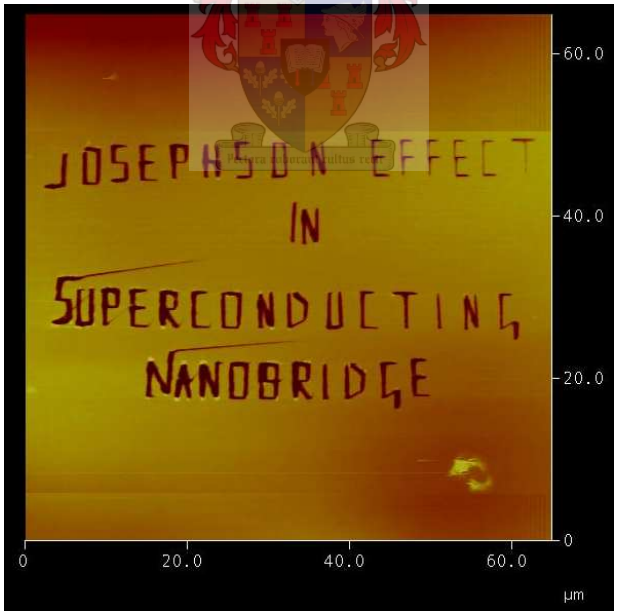

Figure 3.5: Nanolithography on photoresist by AFM.

AFM is widely used all over the world in different areas and fields. In the superconductivity field, it has been used for the analysis of Josephson junctions.

J. Bulman and O. Salazar [42] have studied step-edge junctions with AFM. However, AFM can also be used to fabricate Josephson junctions. S. Yamamoto *et al.* used

lithography to fabricate intrinsic Josephson junctions [43]. I. Song *et al.* fabricated Josephson junctions by inducing selective surface modifications on YBCO strips with the AFM tip [44].

3.3 Pulsed Laser Deposition

The applications of HTS thin films for digital electronic devices require large film areas with highly homogeneous and reproducible superconductive properties. Techniques such as pulsed laser deposition (PLD), *RF* magnetron sputtering, and chemical vapor deposition are very powerful tools in thin film fabrication.

The PLD or laser ablation is used to deposit thin YBCO films on a substrate material. Many attractive features, including the stoichiometric transfer of material from the target, generation of energetic species, and hyperthermal reaction between ablated cations and molecular oxygen in the plasma make the technique popular to deposit an epitaxial thin film. Figure 3.7 shows a basic PLD system.

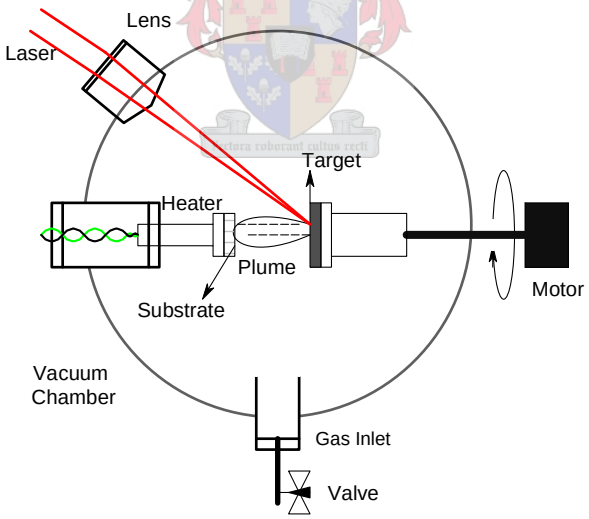

Figure 3.6: Schematic diagram of a pulsed laser deposition system.

In the PLD technique, a pulsed laser is focused onto a rotating target of the material to be deposited in a vacuum chamber.

Each laser pulse vaporizes or ablates a small amount of the material from the target. Many mechanisms are involved when the laser interacts with the target, such as thermal

evaporation of the surface layer and interaction between the electrical field of the beam and the evaporated material. A detailed explanation is however, beyond the scope of this thesis. The laser pulse is absorbed in a thin surface layer.

Due to the high energy density in the interaction region, most of the material will be heated above the evaporation temperature of the layer. The ablated material is ejected from the target into a plasma plume, and deposited onto the hot substrate. Each time the laser pulse hits the target, a layer of the thin film is grown on the substrate and the film growth can be controlled on an atomic level [21].

There are many variable parameters in the PLD technique, such as the laser type, pulse duration and pulse frequency, target properties (e.g., density, melting point, thermal conductivity, and surface morphology), substrate properties (e.g., material, crystallinity, and temperature), the target-substrate geometry [45], the gas purity and pressure, and the post annealing process. The quality of the deposited film is widely influenced by these parameters.

Many groups have reported their ability to produce high quality films, but the deposition parameters used by the individual groups vary greatly.

The drawback of the PLD technique is the presence of micron sized particles in the plasma plume. If these particles are deposited onto the substrate, they will cause problems in the formation of multilayer devices. To reduce the particle density, many techniques have been used including velocity filters to prevent the particles from reaching the substrate, off-axis laser deposition and shadow masks [31].

The National Accelerator Cantre's (NAC) pulsed laser deposition system was used for the fabrication of thin YBCO flims in this work. The system is illustrated in Figure 3.8. Magnesium Oxide (MgO) was used as a substrate material for the thin film fabrication. It acts as a template for the epitaxial growth of YBCO layers. MgO has a low dielectric constant (ε =9.75), which is useful for high frequency applications. It has, however, more lattice mismatch (9%), compared to other substrates, such as $SrTiO_3$ [49].

Figure 3.7: Photo of the NAC pulsed laser deposition system.

Thin YBCO films were prepared on MgO using an XeCI excimer laser with a wavelength of 308 nm and an energy of 275 mJ per pulse. The laser power can be varied by adjusting the voltage on the laser electrodes. The laser is reflected by a mirror before it enters the aperture of the PLD chamber, where it is focused by a lens on a small spot onto the target surface.

The size of the spot is altered by changing the focal length of the lens. The target is tetragonal YBCO, which is mounted in a steel holder and rotated with a constant speed by a stepper motor in order to avoid damage of the target surface by the focused laser beam.

The substrate is attached to the substrate heater with conductive silver paint to ensure a good thermal contact and heated to a temperature of 750^{o}C. The temperature is increased by applying current through the heater element and the amount of current is increased systematically in order not to damage the element. The target-substrate distance is 35 mm. The tip of the plume nearly touches the substrate [48].

The base pressure of the chamber is $\approx 1\times10^{-6}$ mbar and the deposition pressure is 0.4 mbar. The chamber is evacuated with two vacuum pumps used in conjunction with a rotary pump, which is used to remove any contaminants in the chamber before starting the deposition.

The oxygen enters the chamber through an adjustable needle valve. A shutter is placed between the target and the substrate and the laser is triggered at 10 Hz for 5 minutes. This is called pre-ablation and is used to clean the surface layer of the target before the deposition. It is recommended to do this before each run.

The electronic properties of the copper oxide superconductive material show a significant dependence on the oxygen content. Thus, specific oxygen conditions after deposition are required in order to achieve a HTS film [21].
After the deposition, the heater temperature is lowered to 490^{o}C. The chamber is filled with oxygen and the pressure inside the chamber is raised to atmospheric pressure. Hereafter, the thin film is annealed at 490^{o}C for 1.5 h before it is cooled down to room temperature.

3.4 Sample Evaluation

After the PLD was performed, the surface roughness of each the sample was determined with AFM. The superconductivity of the samples was tested by measuring the magnetic flux density inside the samples using a cold finger setup.
The sample was placed between two small coils. One of the coils was driven by a low ac current and the voltage was measured on the other coil. The susceptibility of the sample was monitored by the cryo-cooler measurement system while cooling down the cold finger.
At temperatures below T_c, superconductive samples exhibit the Meissner effect, and no voltage could be measured with the secondary coil. The susceptibility magnitude dropped from 100 to near zero percents. At T_c the susceptibility decreased drastically.

Four point probe measurements could not be performed successfully in this work. Four fine wires were attached on the sample corners; two to bias a small current and the other two to measure the voltage, which was plotted as a function of temperature. The wires were fixed on the surface with silver paste, but the conductivity was lost each time the sample was cooled down.

Photolithography was performed on the samples that were superconductive. This was done as explained in section 3.1, but the exposure time was raised to 25 seconds [31, 35].

3.4 The Etching Process

In this project wet etching was used to etch YBCO samples. It employs chemicals, such as ethylenediaminetetracetic acid (EDTA), hydrochloric acid, nitric acid, or citric acid that reacts with YBCO. The chemical solution used during wet etching in this study was citric acid [31, 46].

A 0.1 mol solution was formed by mixing 10.2 g of citric acid with 500 ml of DI water. The sample was immersed in citric acid in an ultrasonic bath. The time of etching was dependent on the thickness of the YBCO film. Most of the YBCO samples were etched within 40 - 70 seconds. When the substrate under the YBCO layer became visible, the sample was removed from the solution, rinsed in DI water, and checked under the microscope.

The disadvantage of wet etching is the occurrence of under-etching. This occurs when the chemical solution etches the YBCO underneath the photolithography mask, which makes the wet etching not preferable for the etching of small structures.

3.5 Fabrication of Nanobridges

Superconductive YBCO films were patterned into superconductive lines on the substrate with the photolithography and wet etching. Nanobridges were fabricated on the YBCO lines with AFM lithography. A diamond tip scratched across the YBCO line at a specific distance from the center in order to form a constricted area.

This distance was defined in the source code. The tip then indents into the YBCO film and passes across the same region several hundreds of times depending on the desired width of the bridge. The scratched line widths were in the nano-scale.

3.6 Contact Pads and Wire Bonding

It is not possible to solder or bond wires onto the YBCO surface and therefore a layer of silver (Ag) or gold (Au) is deposited to act as contact pads.

Silver and gold do not react with YBCO and they have a small contact resistance. It is important to ensure that the silver layer is thick enough to be used for wire bonding.

Thermal evaporation was used to form the contact pads and thin layers of Ag were deposited on the YBCO surface.

The sample is aligned with a metal mask that has holes where the contact pads should be deposited.

Next the sample is placed inside the vacuum dome. The crucible in the vacuum dome was filled with silver and heated under a high vacuum (10^{-6} mbar). The silver melted and started to evaporate inside the dome. After the evaporation was completed, the sample was annealed at 450^{o}C for 30 minutes in an oxygen atmosphere to from a good adhesion between the silver and the YBCO surface [47].

Figure 3.8 shows one of the samples ready for wire bonding.

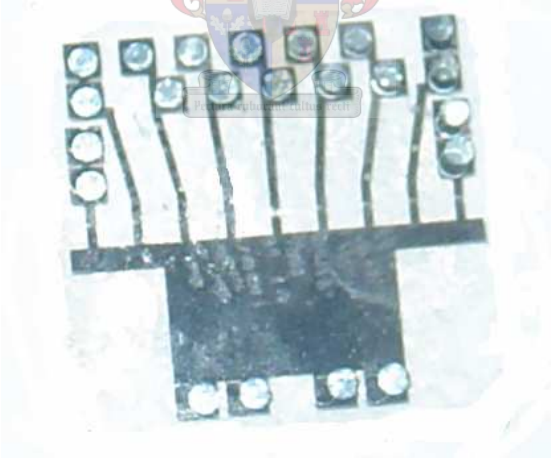

Figure 3.8: YBCO lines with silver contact pads after annealing

Once the annealing was completed, the sample is mounted on a Printed Circuit Board (PCB) after which wire bonding can take place. The contact wires were bonded from the contact pads to the copper strip lines on the PCB board with the ultra-sonic wire bonder in the clean room. The sample was bonded onto the board with silver paste, which

prevents the sample from moving when it is cooled down. Aluminium wire was used to wire the silver contact pads to the PCB.

3.7 Summary

This Chapter describes the fabrication process in detail. The two steps used to improve the sidewall angle of the photoresist lines are photolithography and AFM nanolithography. These two steps were explained in detail.
The scanning and nanolithography features of the AFM were explained, including the two scanning modes that have been used in this work, which are the contact and tapping mode.

The entire process of nanobridge fabrication was explained. The PLD technique used to deposit thin, superconductive YBCO films on MgO substrates was illustrated and the varying parameters in this technique were given. Each of these parameters can change the superconductive properties of the film.
Wet etching, contact pads and wire bonding were also illustrated. These steps were successfully performed as will be seen in the results in Chapter 4.

Chapter 4

Results and Discussion

4.1 Improving the Sidewall Angle of Photoresist Lines

The AFM scanning and lithography orientations on a photoresist line are shown in Figure 4.1. The tip scans from the top left corner to the bottom right corner to determine the sidewall angle of the photoresist line. If the scan rate is too fast, the image will display a wider sidewall angle on the right side of the line, because the feedback of the control is too slow. The right angle is always larger, because of the tilt of the cantilever. Both angles are larger than the real angle because of the tip shape. For this reason, we only improved the left sidewall angle in our experiments. On a few lines, however, the lithography was performed on the right sidewall as well.

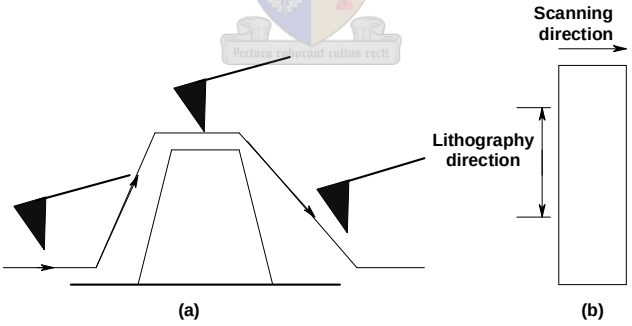

Figure 4.1: Schematic diagrams of the high scanning rate. (a) The tip crossing a photoresist line. (b) Illustrations of the scan and lithography directions.

Silicon and diamond tips were used for nanolithography. The diamond tip did not improve the angle much, due to the geometry of the diamond tip. The diamond coated tip has a wider tip angle. Therefore, sharp silicon tips were mostly used to improve the sidewall angles of the photoresist lines.

The sidewall angle was improved on 78 lines on 24 photoresist samples. The widths of the lines ranged from 4μm to 8μm . Figure 4.2 shows the image of two photoresist lines improved with AFM and the sidewall angle after nanolithography.

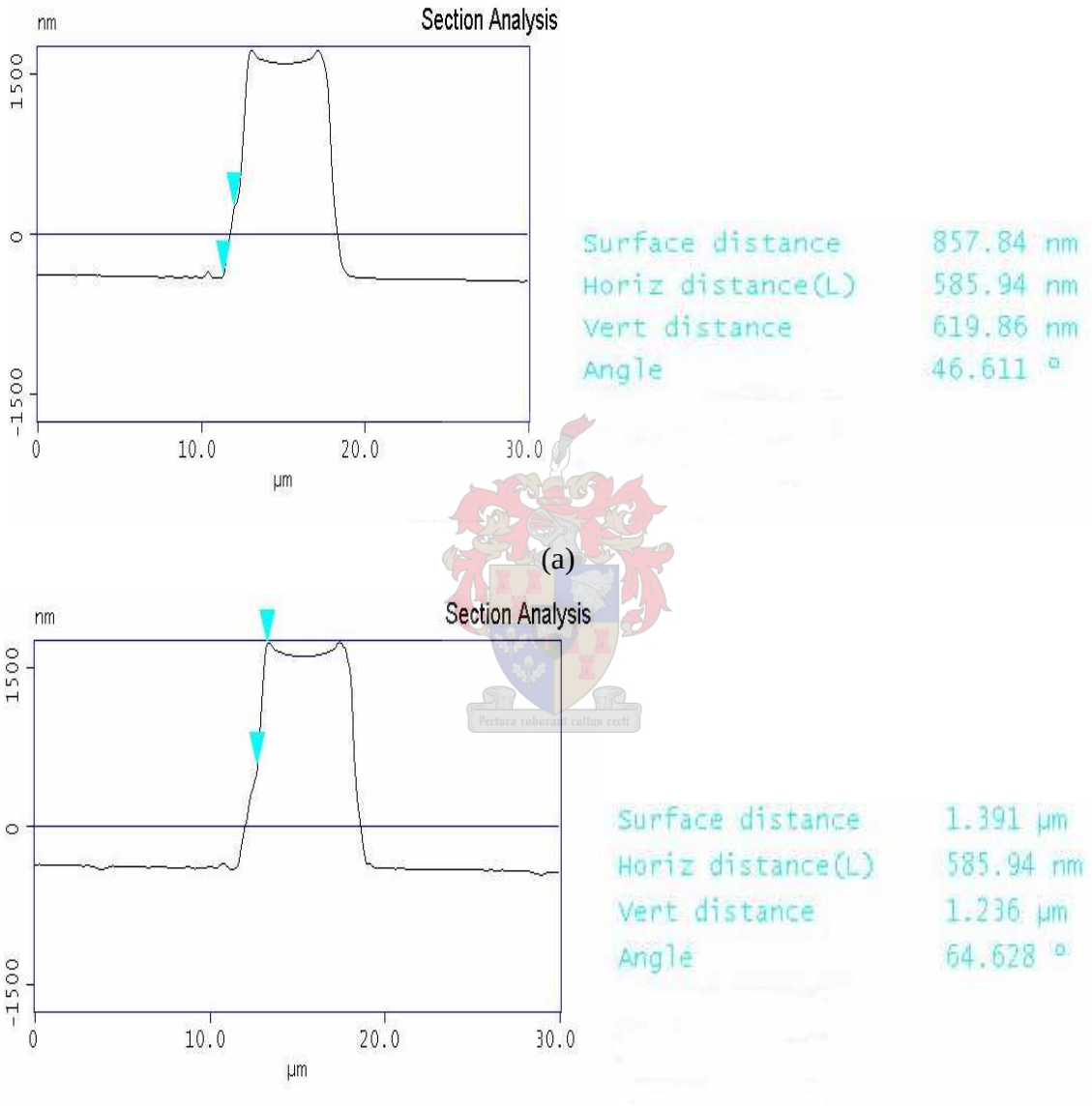

Figure 4.2: Sidewall angle improved with AFM: (a) The original angle is 46.6^{o}. (b) The same angle after lithography is 64.6^{o}.

According to Figures 3.3 and 3.4 the tip angle is about 83°, but this is only a theoretical value. Consequently, if the sidewall angle was improved, it can maximally reach a value of 83°. The measured angle is thus always wider than the real angle, as is illustrated in Figure 4.1. The best angle that could be achieved after improvement was 72°, as illustrated in Figure 4.3.

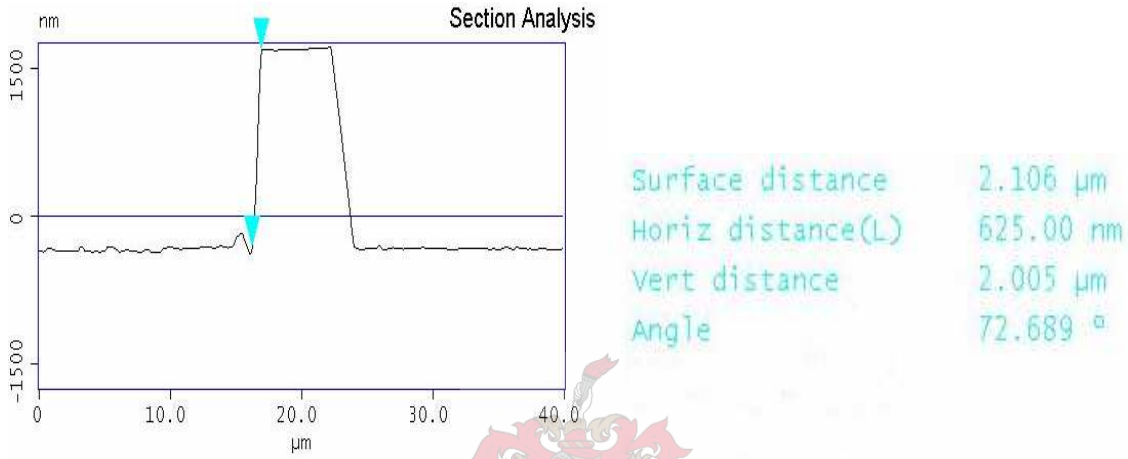

Figure 4.3: The best improvement of a sidewall angle obtained with nanolithography.

The sidewall angle was successfully improved on many lines with various degrees of success. This variation in angles could be explained by the history of the tip. The tips were used to manipulate many samples, which eventually damaged their shape. Also, the cantilever slope from the horizontal plane (Figure 3.3) is a theoretical value that has not been experimentally confirmed.

Samples that were hard baked for a short time (< 20 min) were still soft and contained some solvent in the photoresist. Figure 4.4 shows how those soft resist samples responded to the nanolithography.

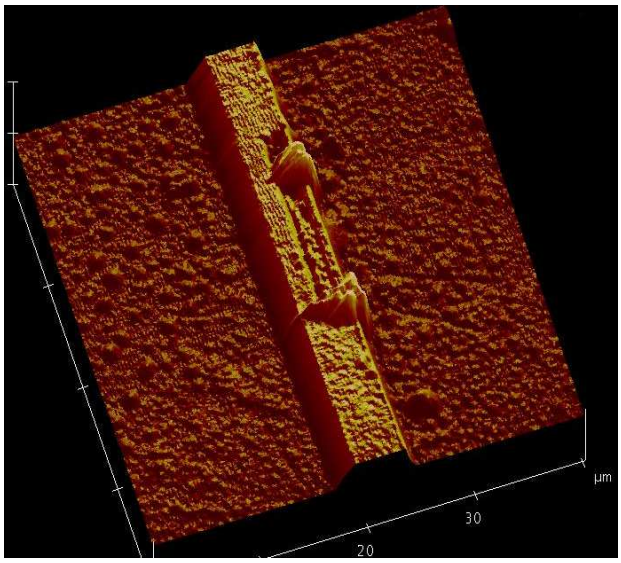

Figure 4.4: Short time hard baked photoresist line after nanolithography.

The scratched material was collected at the end of the scratched lines. This was not the case on samples which were baked for a longer time, because all the solvent was evaporated. Appendix B shows more images of improved sidewall angles on photoresist lines.

4.2 Analysis of the PLD Samples

The morphology of the PLD samples was imaged with AFM, as the surface roughness gives an indication of the quality of the deposited film. High quality films are required to fabricate HTS electronic devices. The superconductive properties of the films were measured with susceptibility tests. Unfortunately, resistivity measurements were not successful as mentioned Chapter 3.

The surface roughness of the YBCO samples that were fabricated with the first set of PLD parameters was 209 nm, which is fairly high. The surface is shown in Figure 4.5a. These parameters were changed, in order to improve the surface roughness of the samples. The laser energy was kept the same but the focal length was changed to vary the laser energy density on the target.

The energy density was determined by measuring the beam energy at the aperture of the chamber divided by the size of the laser beam spot on the target.

The dimensions of the spot were determined by triggering the laser manually on a photographic paper placed on top of the target. The focal length was increased stepwise from minimum to maximum, and at each step the laser was triggered in order to determine the shape of the spot on the photographic paper. A roughly uniform rectangular cross section of the beam was observed with a focal length of 31 - 32 mm. The target-substrate distance was changed in order to maintain the tip of the plume just at the substrate surface. The deposition rate was changed between 2 and 7 Hz.

With a change in the PLD parameters the surface roughness improved, and the optimal parameters [45] resulted a sample with a low surface roughness of 19.3 nm (sample no.5 in Table 4.1), as shown in Figure 4.5b.

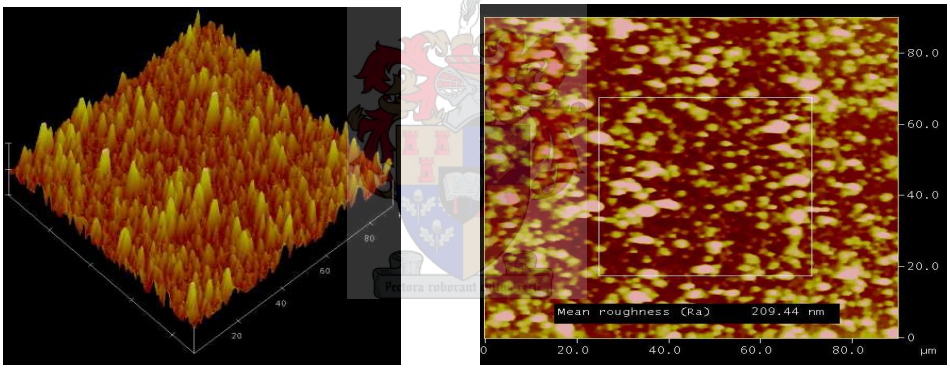

(a)

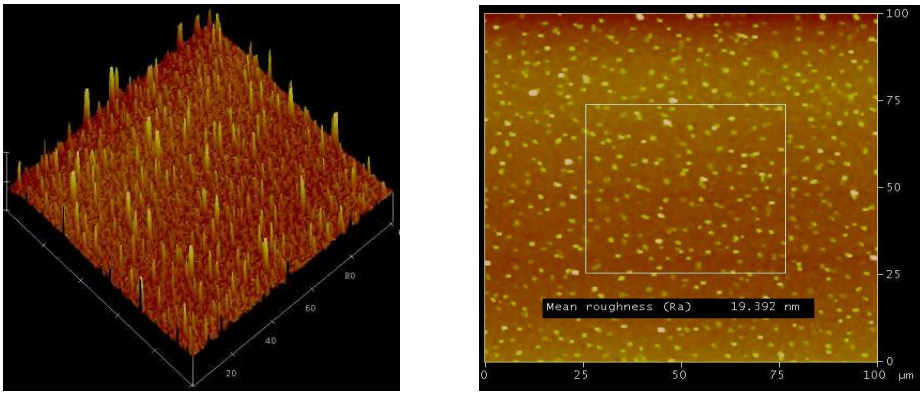

(b)

Figure 4.5: Roughness measurements on two YBCO deposited samples with different PLD settings: (a) Deposition with original parameters. (b) Deposition with optimised parameters.

15 thin YBCO films were deposited with different PLD parameters on MgO substrates, eight of them were superconductive. The superconducting samples had different critical temperatures and different surface roughness values.

Two of the superconductive samples were damaged during the four point resistivity measurements. Four sharp pins attached to springs were used to connect the four corners of the sample surface. When the sample was cooled down, the cold finger was vibrating and the pins consequently destroyed the YBCO film on the substrate.

The nanobridges fabrication was done on five samples. Table 4.1 summarises the PLD parameters for each of them. The susceptibility versus temperature results and surface roughness values for these samples are shown in Figure 4.6.

Table 4.1: The PLD parameters of five superconductive YBCO films used for nanobridges fabrication

Sample Number	Laser Energy at Source (mv)	Laser Pulse Frequency (Hz)	Laser Pulse Density (J/cm^2)	Target-Substrate Distance (mm)	Substrate Temperature (^oC)	Focal Length (mm)	Deposition Pressure (mbar)	Deposition Time (minutes)	Annealing Temperature and time (^oC minutes)
1	600	5	5.4	40	715	31	0.4	15	490 for 30
2	590	7	4.9	42	710	32	0.266	25	480 for 30
3	590	7	4.9	40	720	32	0.266	25	480 for 30
4	600	2	5.1	35	750	32	0.4	80	490 for 60
5	590	7	4.8	41	720	32	0.266	15	480 for 20

(a)

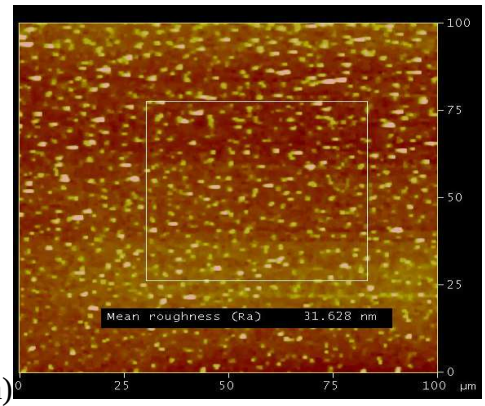
Mean roughness (Ra) 31.628 nm
0
25
50
75
100 µm

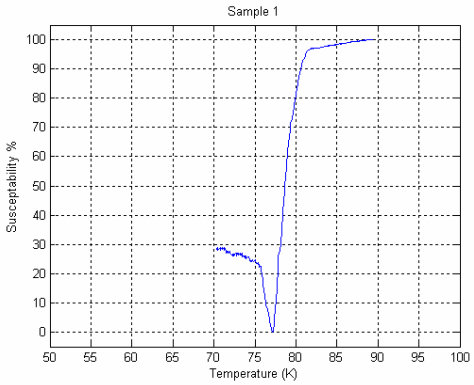
Sample 1
Susceptability %
Temperature (K)

(b)

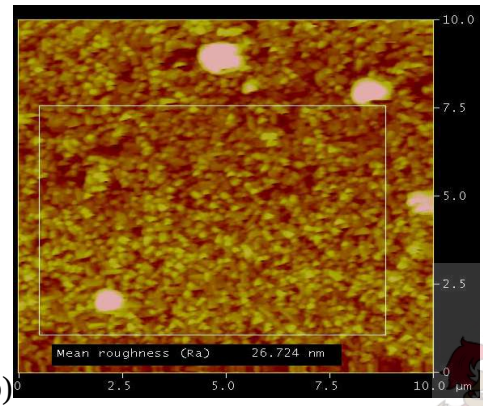
Mean roughness (Ra) 26.724 nm
0
2.5
5.0
7.5
10.0 µm

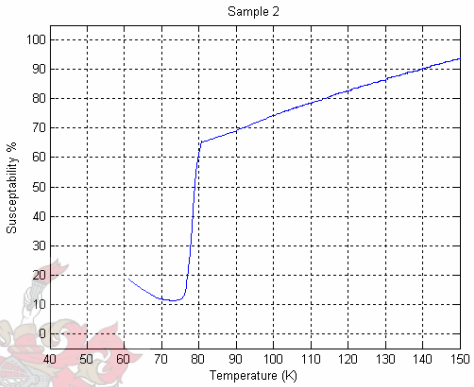
Sample 2
Susceptability %
Temperature (K)

(c)

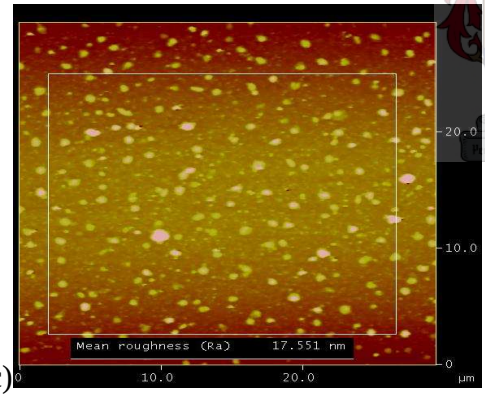
Mean roughness (Ra) 17.551 nm
0
10.0
20.0 µm

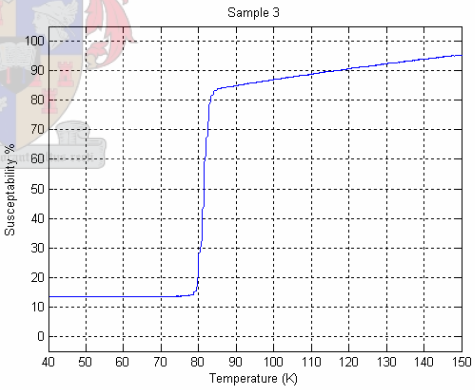
Sample 3
Susceptability %
Temperature (K)

(d)

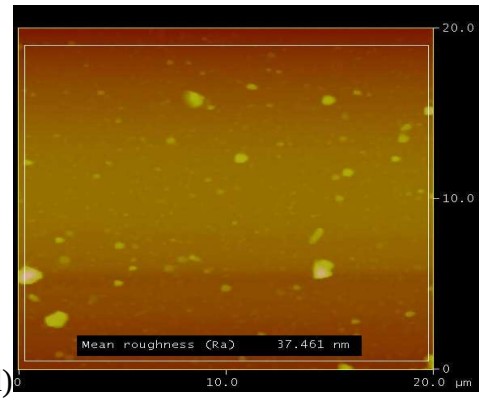
Mean roughness (Ra) 37.461 nm
0
10.0
20.0 µm

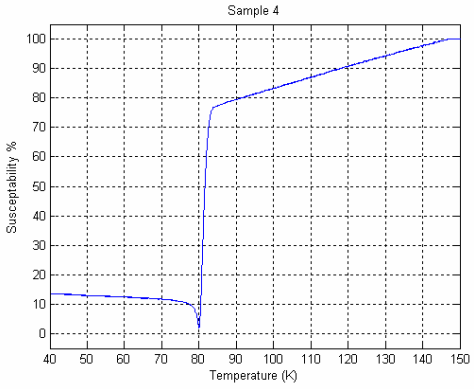
Sample 4
Susceptability %
Temperature (K)

(e) 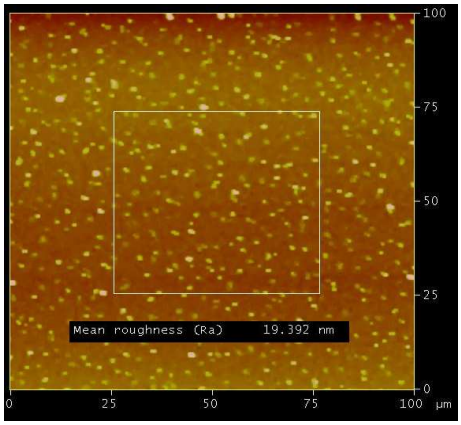

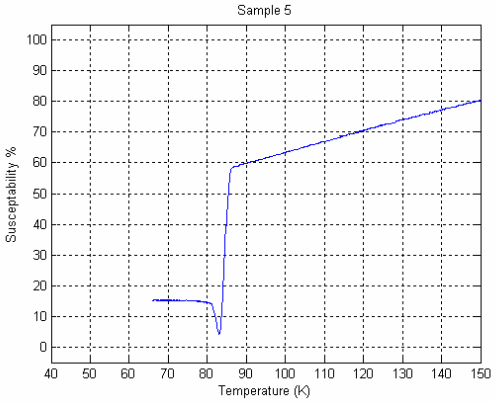

Figure 4.6: Roughness and Susceptibility measurements of the five superconductive samples used for the fabrication of nanobridges.

Sample number 5 (Figure 4.6 e) shows the best values compared to the others, as it has the best surface roughness (19.39 nm) and transition temperature width of less than 3 K starting at 86 K.

It can be seen in the susceptibility results that the responses of the samples below the transition temperatures are different. This is because some components of the cryo-cooler electronics were replaced between the samples measurements. The probe sensor was damaged while changing the sample holder of the cryo-cooler. The sensor was changed and the temperature was calibrated with a reference YBCO sample that was purchased from an overseas supplier.

Appendix C shows the settings and the results for the other PLD samples, including the non-superconductive samples.

4.3 Wet Etching Results

Figure 4.7 shows AFM images of the samples after being wet etched. Figure 4.7a shows the sample with the photoresist still on top of the wet etched YBCO line. Figure 4.7b shows the sample after removal of the photoresist with acetone. Figure 4.7c shows a wet etched SQUID with photoresist on top. Figure 4.7d shows a wet etched SQUID where under-etching occurred due to a too long etching time.

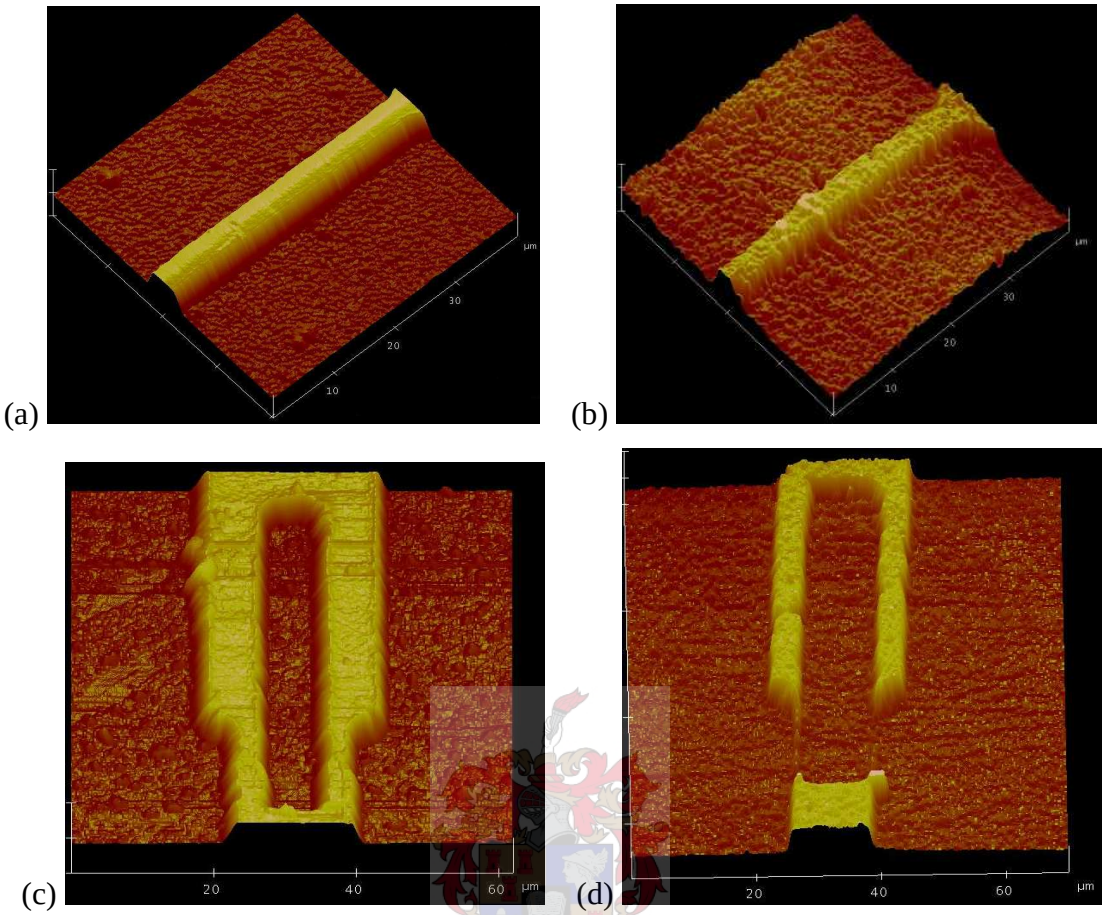

Figure 4.7: AFM images of wet etched samples: (a) YBCO line with photoresist still on top. (b) Without photoresist. (c) SQUID with photoresist. (d) SQUID under-etched.

The problem with wet etching is that there is no specific time at which the etching is stopped. It depends on the sample thickness. The sample is etched for a few seconds and then evaluated visually or under the microscope, as is illustrated in Figure 4.8.

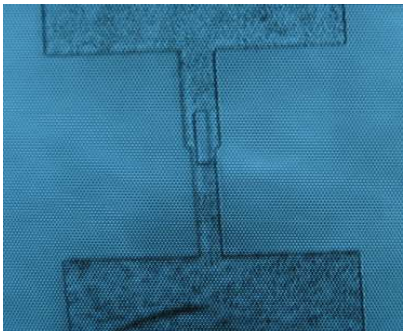

Figure 4.8: Wet etched sample under the optical microscope.

4.4 The Final Circuit Tests and Results

On the five superconductive samples 34 YBCO lines were constricted with nanolithography to form nanobridges. Examples of these bridges are shown in Figure 4.9.

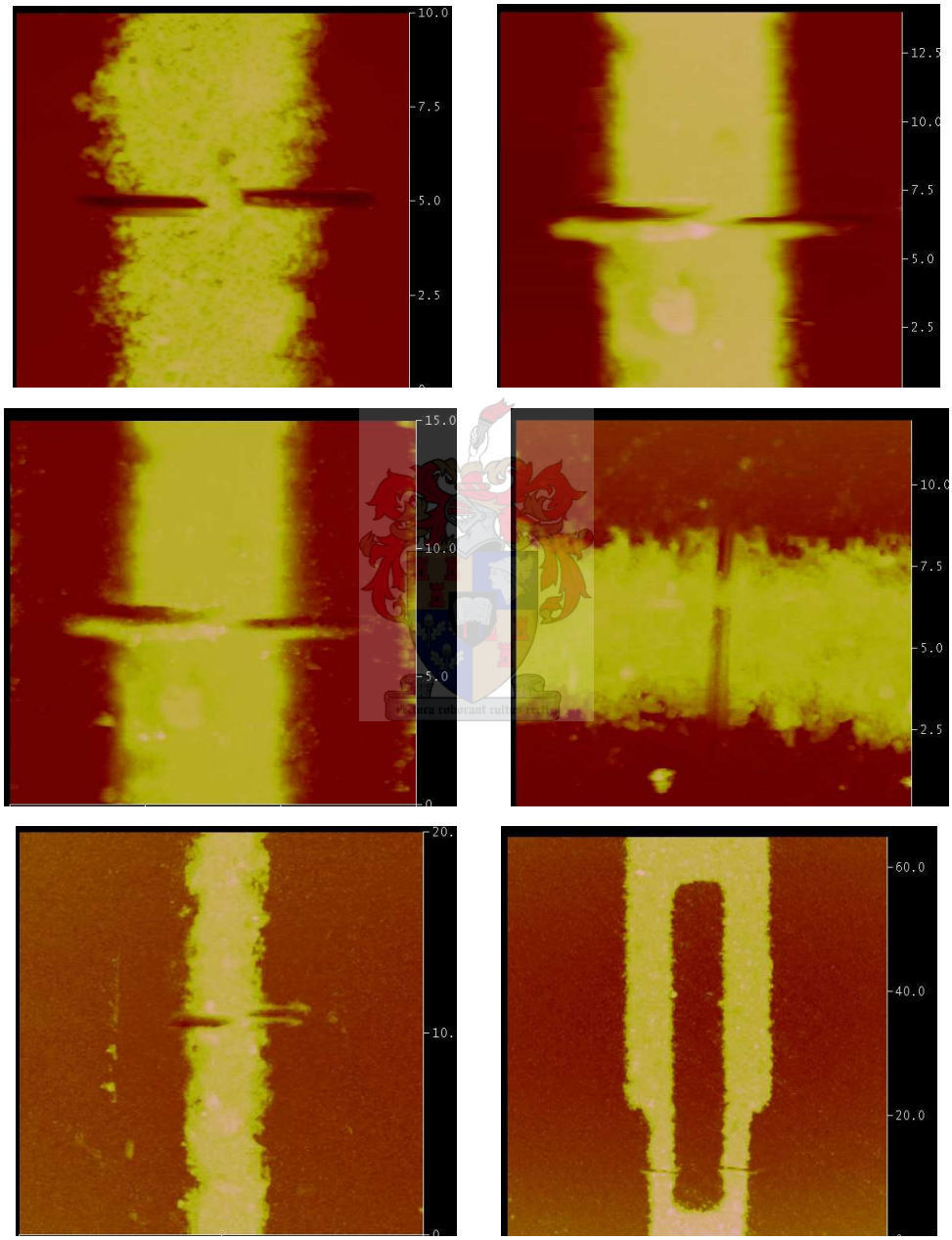

Figure 4.9: YBCO lines constricted with AFM nanolithography.

The thickness of the YBCO films was between 140 nm and 530 nm. Bridges with lengths between 370 nm to$1.5\,\mu$m and widths between 250 nm to $3.4\,\mu$m have been fabricated on these samples.

Several of these constrictions had the potential to exhibit Josephson behaviour (Section 2.6.4 in Chapter 2). Their sizes were comparable to the effective penetration depth in YBCO, $\lambda_{eff} = \lambda_L \cot h\left(d/2\lambda_L\right) \approx 2\lambda/d$, where d is the thickness of the sample and λ in YBCO is about 170 nm at 87 K [1].

The constricted YBCO lines were wire bonded to a printed circuit board. Two wires for bias current and two wires to measure the voltage across the bridge were connected.

In order to display an I-V curve of the junctions, a triangular current was applied to the bridge using a Mr SQUID measurement unit [50]. Mr SQUID can supply a low triangular current waveform, and contains a low noise amplifier, which amplifies the voltage signal. The oscilloscope is set to the XY display mode, the triangular current is connected to one channel and the voltage across the bridge is connected to the other channel.

The samples were cooled in two ways: either immersion in liquid nitrogen, or cooling with a cryo-cooler. Figure 4.10 shows both methods.

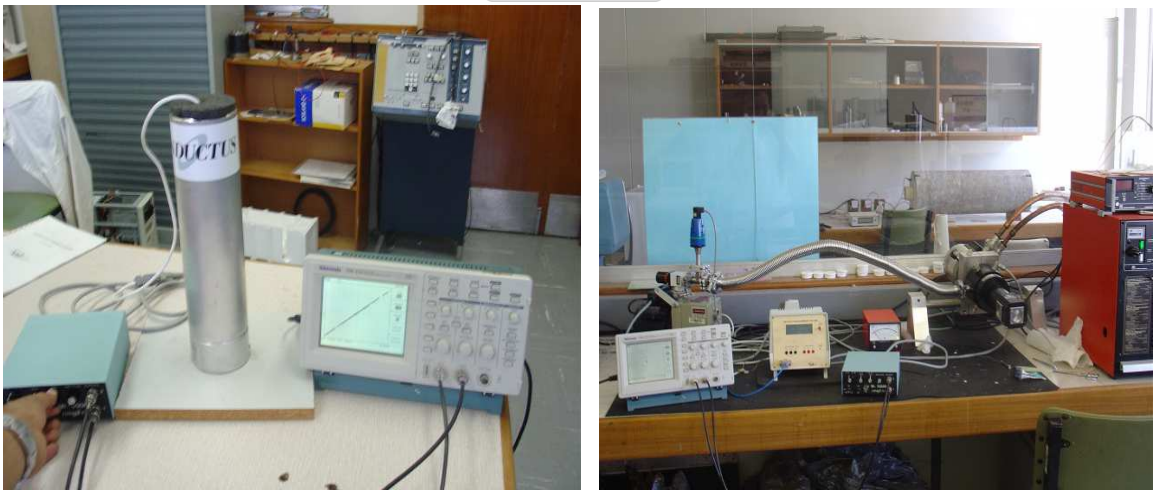

(a) (b)

Figure 4.10: Samples were tested in: (a) liquid nitrogen, or (b) A cryo-cooler system

Unfortunately, none of the bridges exhibited Josephson behaviour. The I-V curves remaind unchanged in all the samples. The wire bonding was checked by measuring the conductivity between the four wires that connected the bridge to the board through external wires, which indicated no loss.

All YBCO lines had lost their superconductivity during the process. This could be due to the thermal instability of the samples. The superconductive properties in HTS thin films are very sensitive and are affected by the oxygen content and also the position of the atoms in the YBCO structure.

Up to this point, it is not known at which step of the entire process the superconductivity was lost. To verify this, a superconductive sample (that none of the process steps was performed on it) was annealed again at 480^{o}C for 30 minutes at the PLD after the susceptibility measurement. The sample lost its superconductivity after the annealing process. Figure 4.11 shows the susceptibility measurements of the superconductive sample before and after the annealing.

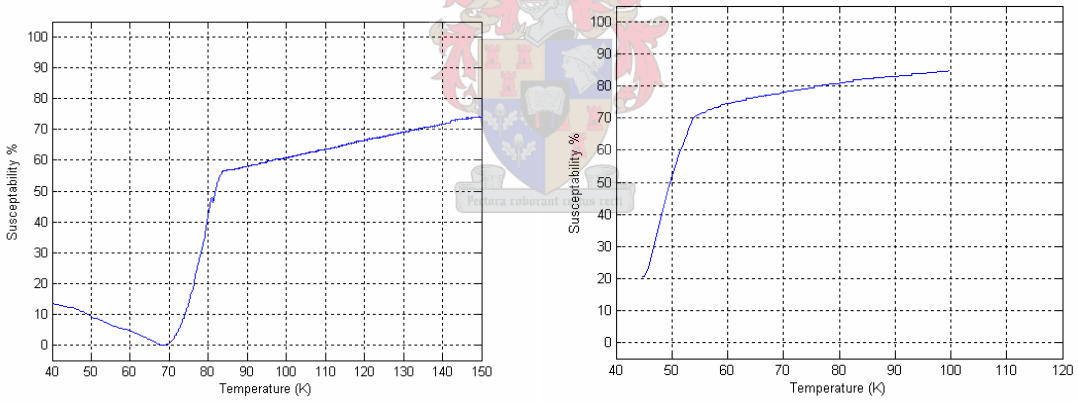

(a) (b)

Figure 4.11: Susceptibility measurement on: (a) Superconductive sample. (b) Same sample after annealing.

The CuO_2 plane in the HTS crystal structure is the conduction plane which is responsible for superconductivity. Hence, a small change in oxygen content can transform material from superconductive to metallic or isolative [21].

4.5 Summary

In this Chapter the results from each manufacturing step are shown. The improvement of the sidewall angle of the photoresist lines was illustrated with AFM images. The best improved angle that could be achieved was 72^{o}. The AFM nanolithography was successfully performed on most of the photoresist lines.

The thin YBCO films that resulted from the PLD technique were imaged. The improvements of the surface roughness, as well as the critical temperature of the films, were illustrated by AFM images and the susceptibility tests. The surface roughness was improved from 209 nm to 19.39 nm. The films were improved from non-superconductive into superconductive with a critical temperature of 86 K and transition temperature width of less than 3 K, as illustrated in Figure 4.6e.

Reproduced results from wet etching and wire bonding were achieved. The conductivity had not been lost during the test of the final circuits, which indicates a good performance of the wire bonding process.

The desired dimensions of the nanobridge were achieved with the AFM nanolithography. Constrictions with sizes comparable to the effective penetration depth in YBCO were fabricated.

Chapter 5

Conclusions and Recommendations

5.1 Conclusions

The primary objective of this project was to improve the sidewall angle of photoresist lines. This was successfully achieved with the AFM nanolithography. Several sidewalls angles of photoresist lines were improved. Angles that previously ranged from 47^{o} to 53^{o} were steepened up to 68^{o}. The best improved angle achieved was 72^{o}.

The second objective was to fabricate HTS nanobridges. This was achieved by constricting superconductive YBCO lines with AFM nanolithography. Several bridges with sizes comparable to the effective penetration depth of $YBa_2Cu_3O_7$ films were fabricated. The length and the width of the bridges were manipulated with AFM nanolithography in order to obtain the desired dimensions.

Wet etching was performed with reproducible results, although under-etching was observed on a few lines. The contact pads were deposited on the thin film using a thermal evaporation method. The contact pads were thick enough for successful wire bonding.

Unfortunately, the nanobridges did not show any Josephson behaviour. The I-V curves did not change when the samples were cooled to low temperatures, because the samples lost their superconductivity. This problem was reported before [31].

The samples retrieved from the PLD system were not thermally stable and the oxygen level and structure in the YBCO samples were affected by the annealing process. This could be proved by annealing a thin superconductive film in the PLD system, before performing any one of the process steps on it. This film lost its superconductive properties, because its structure changed. The film changed from the orthorhombic phase (superconductive phase) to the tetragonal phase, which inhibited superconductivity.

5.2 Recommendations

To fabricate HTS Josephson junctions with the available facilities several aspects should be addressed.

The photolithography process needs to be optimised. Procedures such as characterization of the photoresist profile, finding the optimal soft and hard bake, exposure and development times need to be studied and more experiments need to be performed in order to define standard parameters for successful UV photolithography.

The influence of the sidewall angle and the hardness of the photoresist can be further improved in order to successfully fabricate step edge junctions.

Wet etching of samples can be monitored with AFM to prevent under-etching, or a database can be created for the etching time versus YBCO film thickness.

For better results from the PLD system, few parameters need to be study. The focal lens is important in order to focus the laser beam on the target. With the maximum and minimum limits of the focal lens in the system at this stage, a uniform rectangular cross-section profile of the laser beam could not be achieved on the target surface. To obtain a excellent plasma plume from the target to produce a smooth film, a uniform laser energy density is required.

Additional methods to characterize superconducting thin films are available which have not been used in this thesis. Methods like four-point resistivity measurements can provide more insight about the film properties such as critical current and temperature. To determine the growth orientation of the film, X-ray diffraction is needed.

References

[1] C. P. Poole, H. A. Farach, R. J. Creswick, *Superconductivity*, Academic Press. 1995.

[2] J. D. Doss, *Engineer's Guide to High-Temperature Superconductivity*, John Wiley & Sons, 1989.

[3] M. K. Wu, J. R. Ashburn, C. J. Torng, P. H. Hor, R. L. Meng, L. Gao, Z. J. Huang, Y. Q. Wng, and C. W. Chu, "Superconductivity at 93 K in a new mixed-phase Yb-Ba-Cu-O compound system at ambient pressure," *Physical Review letters*, vol. 58, no. 9, pp. 908 – 910, 1987.

[4] L. Gao, Y. Y. Xue, F. Chen, Q. Xiong, R. L. Meng, D. Ramirez, C. W. Chu, J. H. Eggert, and H. K. Mao, "Superconductivity up to 164 K in $HgBa_2Ca_{m-1}Cu_mO_{2m+2+\delta}$ (m=1, 2, and 3) under quasihydrostatic pressures," *Physical Review B*, vol. 50, pp. 4260-4263, 1994.

[5] T. P. Orlando, and K. A. Delin, *Foundations of Applied Superconductivity*, Addison-Wesley Publishing Company, 1991.

[6] A. M. Kadin, *Introduction to Superconducting Circuits*, John Wiley & Sons, 1999.

[7] A. A. Abrikosov, "On the magnetic properties of superconductors of the second group," *Soviet Physics, JETP*, vol. 5, pp. 1174 – 1182, 1957.

[8] W. J. Perold, M. Jeffrey, Z. Wang, T. Van Duzer, "Complementary output switching logic - a new superconducting voltage-state logic family," *IEEE Transactions on Applied Superconductivity*, vol. 6, no. 3, pp. 125 - 131, 1996.

[9] M. Jeffrey, W. Perold, T. Van Duzer, "Superconducting complementary output switching logic operating at 5-10 Gb/s," *Applied Physics Letters*, vol. 69, no.18, pp. 2746 - 2748, 1996.

[10] C. J. Fourie, "A 10 GHz oversampling delta modulating analogue-to-digital converter implemented with hybrid superconducting digital logic," Msc Thesis, University of Stellenbosch, 2001.

[11] Hypres, 175 Clearbrook Road, Elmsford, New York 10523, home page: http://www.hypres.com

[12] R. Doll and M. Näbauer, "Experimental proof of magnetic flux quantization in superconducting ring", *Physical Review letters*, vol. 7, pp. 51 - 52, 1961.

[14] U. Essman and H. Trauble, "The direct observation of individual flux lines in type II superconducting", *Physics Letters A*, vol. 24, no. 10, pp. 526 - 527, 1967.

[15] K. K. Likharev, *Dynamics of Josephson Junctions and Circuits*, Gordon and Breach Science Publishers, 1986.

[16] B. D. Josephson, "Possible new effects in superconducting tunneling", *Physical Review Letters*, vol. 1, no. 7, pp. 251-253, 1962.

[17] R. Rottier, "Establishing a process for the fabrication of high-quality HTS SQUIDs", Msc Thesis, University of Stellenbosch, 2003.

[18] P. W. Anderson and J. M. Rowell, "Probable observation of the josephson superconducting tunneling effect," *Physical Review Letters*, vol. 10, no. 6, pp. 230 – 232, 1963.

[19] K. K. Likharev, "superconducting weak link," *Review Modern Physics*, vol. 51, no.1, pp. 101 - 159, 1979.

[20] R. Gross, L. Alff, A. Beck, O.M. Froelich, D. Koelle, and A. Marx, "Physics and technology of high temperature superconducting josephson junctions", *IEEE transactions on Applied Superconductivity*, vol. 7, no. 2 , pp. 2929 - 2934, 1997.

[21] N. Khare, *Handbook of High-Temperature Superconductor Electronics*, Marcel Dekker, 2003.

[22] K. K. Likharev, "Vortex motion and the Josephson effect in superconducting thin bridges", *Soviet Physics JETP*, vol. 34, no. 4, pp. 906 - 912, 1972.

[23] L. G. Aslamazov and A. I. Larkin, "Josephson effect in wide superconducting bridges", *Soviet Physics JETP*, vol. 41, no. 2, pp. 381 - 386, 1975.

[24] M. J. M. E. de Nivelle, G. J. Gerritsma, and H. Rogalla, "Thermally activated coherent vortex motion in $YBa_2Cu_3O_{7-\delta}$ thin film microbridges", *Physical Review Letters*, Vol. 70, pp. 1525 - 1528, 1993.

[25] J. Schneider, M. Mück, and R. Wördenweber, "DC SQUIDs based upon $YBa_2Cu_3O_7$ nanobridges", *Applied Physics Letters*, vol. 65, no. 19, pp. 2475 - 2477, 1994.

26- M. Faucher *et al*., "Niobium and niobium nitride SQUIDs based on anodized nanobridges made with an atomic force microscope", *Physica C*, vol. 368, no. 1, pp. 211 - 217, 2002.

[27] S. K. Lam and D. L. Tilbrook, "Development of a niobium nanosuperconducting quantum interference device for the detection of small spin populations", *Applied Physics Letters*, vol. 82, no. 7, pp. 1078 - 1080, 2003.

[28] J. Schneider, A. V. Hart and R. Wordenweber, "Superconducting flux-flow transistors based upon YBa2Cu_3O_7 nanobridges", *IEEE transactions on Applied Superconductivity*, vol. 5, no. 2, pp. 3393 - 3396, 1995.

[29] D. H.A. Blank, W. Booij, H. Hilgenkamp, B. Vulink, D. Veldhuis, and H. Rogalla, "$YBa_2Cu_3O_7$ Nnno-bridge junctions and dc SQUIDs made by focused ion beam milling", *IEEE transactions on Applied Superconductivity*, vol. 5, no. 2 , pp. 2786 - 2789, 1995.

[30] M. V. Pedyash, D. H.A. Blank, J. H. Muijnck, and H. Rogalla, "Properties of YBaCuO Nanobridges and dc SQUIDs", *IEEE transactions on Applied Superconductivity*, vol.7, no.2 , pp. 2764 - 2767, 1997.

[31] F. W. Graser,"A reproducible process to design and manufacture squid magnetometers", Msc thesis, University of Stellenbosch, 2004.

[32] Vossen, J.L (1978), Thin Film Processes. Academic Press Inc, Orlando, Florida. ISBN 0-12-728250-5.

[33] www.eng.yale.edu / rslab/resources/s1800 series datasheet.pdf

[34] www.lpm.u-nancy.fr/webperso/nanomag/applreils/litho-oc/002photolithmanual.pdf.

[35] L. Snetler, "High temperature superconducor step edge fabrication for the implementation of rsfq circuits", Msc thesis, University of Stellenbosch, 2004.

[36] G. Binnig, C. F. Quate, C. Gerber. "Atomic force microscope", *Physical Review Letters*, vol. 56, pp. 930 - 933, 1986.

[37] L. A. Bottomley, J. E. Coury, and P. N. First. "Scanning probe microscopy", *Analytical Chemistry*, vol. 68, no.12, pp.185 – 230, 1996.

[38] A. Klash, "Identifying different crystallion forms of isotactic polypropylene with atomic force microscopy", Msc thesis, University of Stellenbosch, 2006.

[39] Kopniczky, “Nanostructures studied by AFM. Ion tracks and nanotextured films”, comprehensive summaries of Uppsala dissertations from Faculty of Science and Technology, 905, pp. 58, Uppsala. ISBN 91-554-5795-9.

[40] F. J. Giessibl, “Advances atomic force microscopy”, *Review Modern Physics*, vol. 75, no. 3, pp. 949 – 983, 2003.

[41] Nanolithography software version 5.12, Digital Instruments, Veeco Metrology Group, 2001.

[42] J. B. Bulman and O. O. Salazar, “AFM analysis of step-edge Josephson junctions”, *IEEE transactions on Applied Superconductivity*, vol. 7, no. 2 , pp. 3650 - 3653, 1997.

[43] S. Yamamoto, A. Kawaguuchi, S. Oda, “Anomalous current-voltage characteristics along the c-axis in YBaCuO thin films prepared by MOCVD and AFM lithography”, *Physica C*, vol. 293, pp. 244-248, 1997.

[44] I. Song, B. M. Kim, G. Park, “Fabrication of a Josephson junction using an atomic force microscopy”, *Applied Physics Letters*, vol. 76, no. 5, pp. 601 – 603, 2000.

[45] S. F. Xu, Y. J. Tian, “the effect of laser energy density and target-substrate distance on the quality of YBCO thin films”, *Superconductor Science and Technology*, vol. 7, pp 435 – 437, 1994.

[46] E. H. Conradie, ‘The design and fabrication of dc SQUID magnetometers”, Msc thesis, University of Stellenbosch, 1998.

[47] J. W. Ekin, C. C. Clickner, ”Oxygen Annealing of Ex-Situ YBCO/Ag thin-film interface”, *IEEE transactions on Applied Superconductivity*, vol. 5, no. 2 , pp. 2400 - 2403, 1995.

[48] E. H. Lee, S. J. Park, I. H. Song, I. Son, J. G. Hug, J. Sok, and J. W. Lee, “fabrication of high quality YBCO thin flims using PLD”, *IEEE transactions on Applied Superconductivity*, vol. 7, no. 2 , pp. 1193 - 1196, 1997.

[49] J. M. Phollips, “Substrate selection for high temperature superconducting thin films”, *Journal of Applied Physics*, vol. 79, no.4, pp. 1829 – 1848, 1996.

[50] Conductus, Inc., 969 West Maude Avenue, Sunnyvale, California, 94086, USA, Mr.SQUID User’s Guide.

Appendices

Appendix A

AFM Nanolithography Program Example

```
// diamond.cpp
// Example #1 - Writing a Lithography Program

#include <litho.h>

extern "C" __declspec(dllexport) int macroMain()
{
	LITHO_BEGIN

	LithoDisplayStatusBox();	// display litho status box

	LithoScan(false);		// turn off scanning
	LithoCenterXY();		// move tip to center of field

	double size = 10;		// 10 um from center of diamond to point
	double rate = 20;		// move the tip in X-Y at 20 um/s

	double depth = -0.020;		// push the tip in 20 nm to draw lines
	double z_rate = 0.040;		// move the tip down at 40 nm/s

	// move to left side of the line.
	LithoTranslate( size, 0, rate);		// move the tip 10 um in X-direction

	// push tip into surface
	LithoMoveZ(depth, z_rate);	// moving in Z turns off feedback

	// scribe four sides of the diamond
	LithoTranslate(0, size, rate);		// move the tip 10 um in Y-direction
	LithoTranslate(0, -size, rate);		// move the tip -10 um in Y-direction
	LithoTranslate(0, -size, rate);		// move the tip 10 um in Y-direction
	LithoTranslate( 0, size, rate);		// move the tip -10 um in Y-direction

	LITHO_END

	return 0;	// 0 makes the macro unload. Return 1 to keep the macro loaded.
```

Appendix B

Images of Improved Sidewall Angles

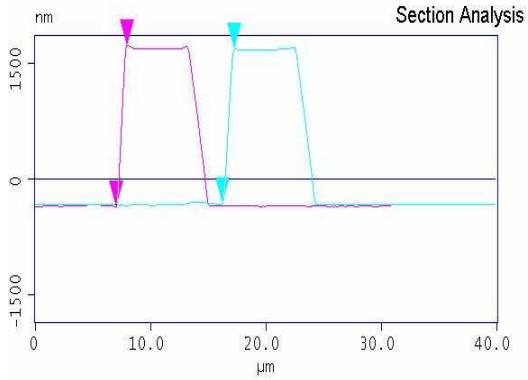

Surface distance	2.256 µm
Horiz distance(L)	937.50 nm
Vert distance	2.012 µm
Angle	65.019 °
Surface distance	2.392 µm
Horiz distance	937.50 nm
Vert distance	2.093 µm
Angle	65.869 °

Spinning time (seconds)	Soft bake (minutes @ 115°C)	Exposure time (seconds)	Development time (seconds)	Hard bake time (minutes)
4500	3	15	40	30

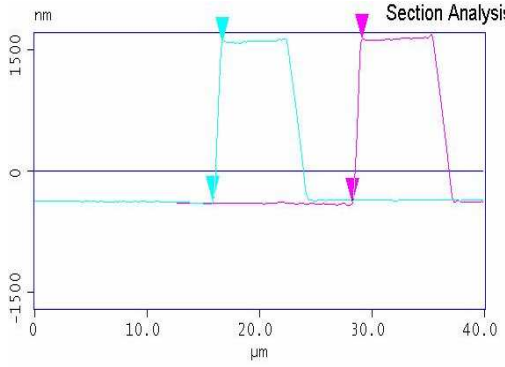

Surface distance	2.330 µm
Horiz distance(L)	937.50 nm
Vert distance	2.011 µm
Angle	65.008 °
Surface distance	2.233 µm
Horiz distance	781.25 nm
Vert distance	2.031 µm
Angle	68.962 °

Spinning time (seconds)	Soft bake (minutes @ 115°C)	Exposure time (seconds)	Development time (seconds)	Hard bake time (minutes)
4500	3	15	40	30

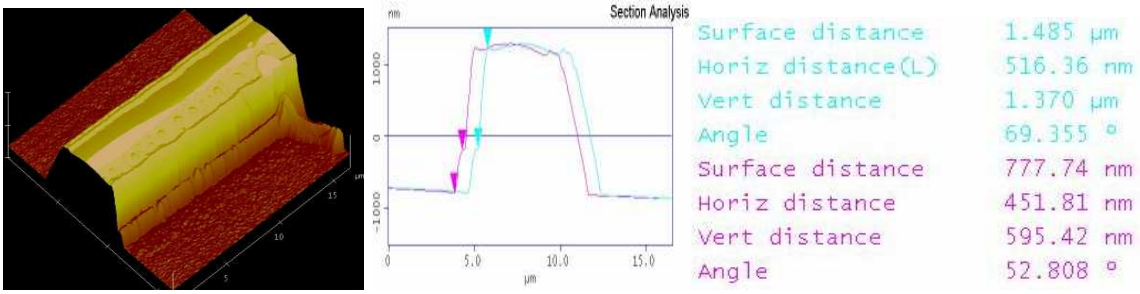

Spinning time (seconds)	Soft bake (minutes @ 115°C)	Exposure time (seconds)	Development time (seconds)	Hard bake time (minutes)
4800	2	15	45	20

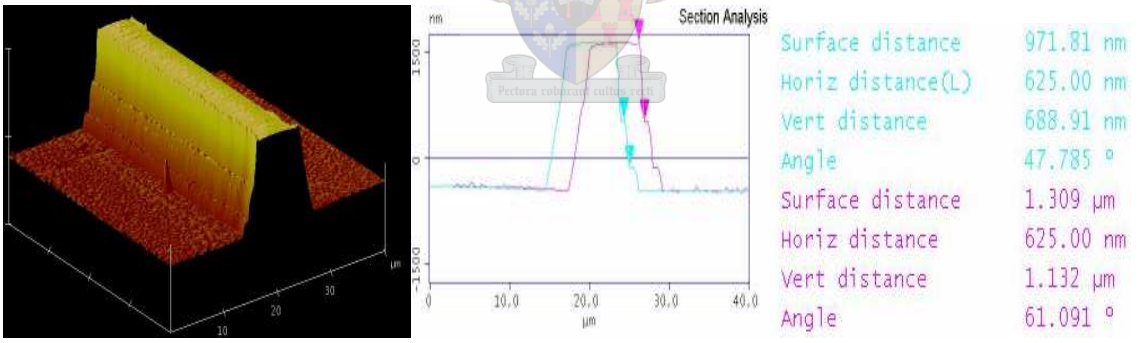

Spinning time (seconds)	Soft bake (minutes @ 115°C)	Exposure time (seconds)	Development time (seconds)	Hard bake time (minutes)
4800	2.5	15	45	35

Appendix C

PLD Thin YBCO Films

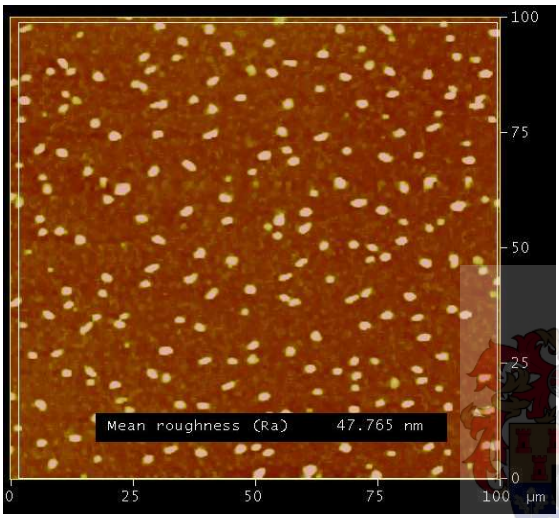

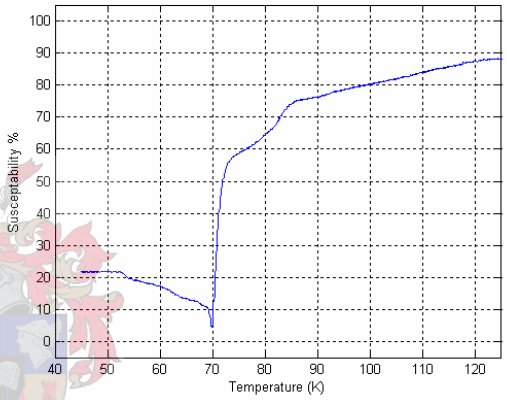

Laser Energy (mJ)	Deposition Parameters (Hz for min)	Target-Substrate distance (mm)	Substrate Temperature (^{o}C)	Focal Length (mm)	Deposition Pressure (mbar)	Annealing Parameters (Hz for min)
275	7 for 90	42	750	31	0.3	490 for 60

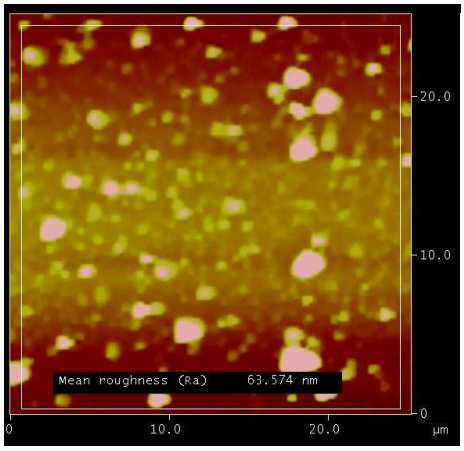

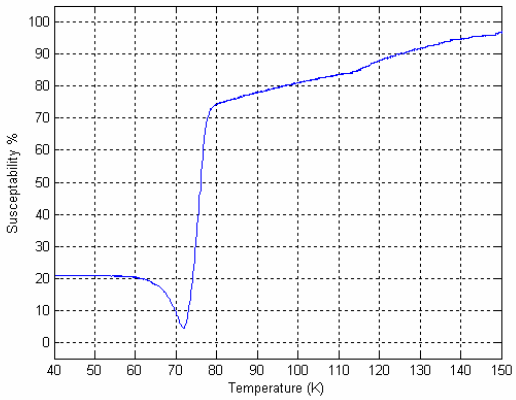

Laser Energy (mJ)	Deposition Parameters (Hz for min)	Target-Substrate distance (mm)	Substrate Temperature (^{o}C)	Focal Length (mm)	Deposition Pressure (mbar)	Annealing Parameters (Hz for min)
240	5 for 60	42	750	31	0.3	490 for 60

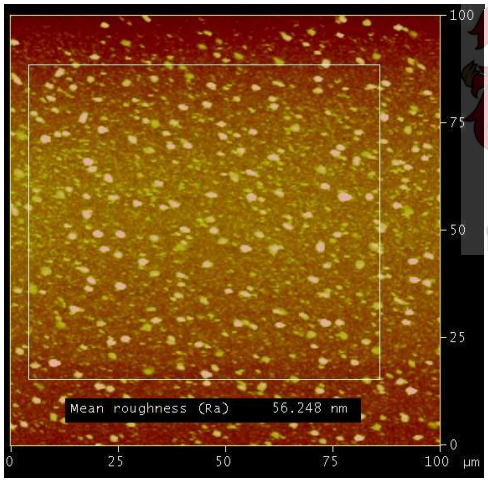

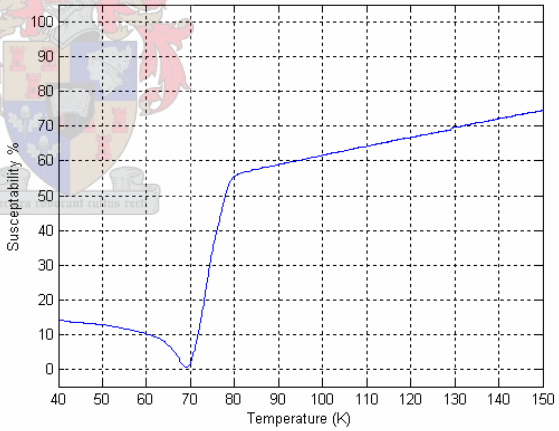

Laser Energy (mJ)	Deposition Parameters (Hz for min)	Target-Substrate distance (mm)	Substrate Temperature (^{o}C)	Focal Length (mm)	Deposition Pressure (mbar)	Annealing Parameters (Hz for min)
275	3 for 30	41	725	32	0.4	490 for 40

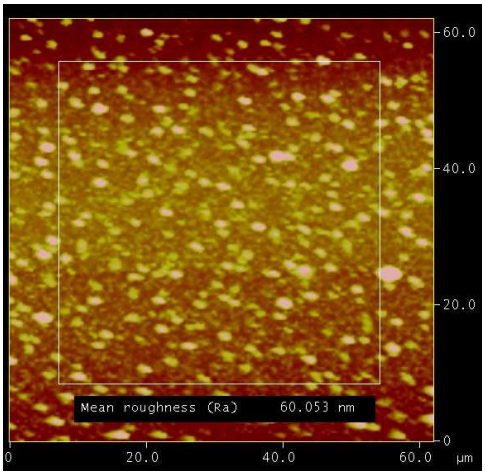

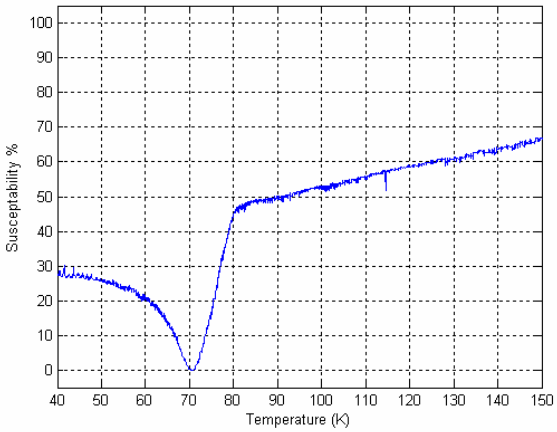

Laser Energy (mJ)	Deposition Parameters (Hz for min)	Target-Substrate distance (mm)	Substrate Temperature (^{o}C)	Focal Length (mm)	Deposition Pressure (mbar)	Annealing Parameters (Hz for min)
268	10 for 5	41	720	32	0.4	490 for 40

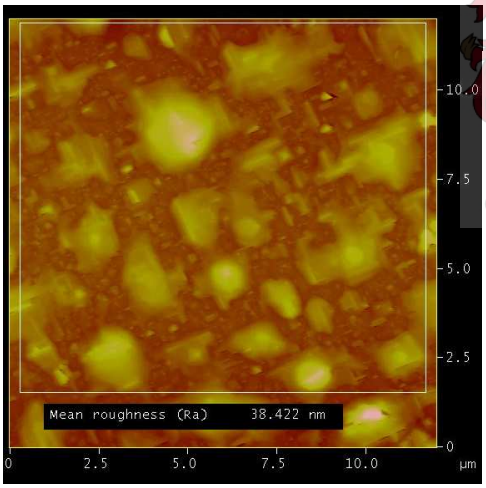

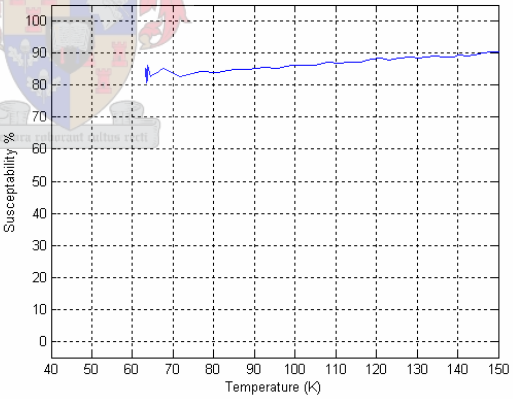

Laser Energy (mJ)	Deposition Parameters (Hz for min)	Target-Substrate distance (mm)	Substrate Temperature (^{o}C)	Focal Length (mm)	Deposition Pressure (mbar)	Annealing Parameters (Hz for min)
275	7 for 70	48	750	32	0.266	530 for 25